

Utah State University

DigitalCommons@USU

All Graduate Theses and Dissertations

Graduate Studies


5-2015

Optical Characterization of Carbon Nanotube Forests

Brian D. Wood

Utah State University

Follow this and additional works at: <https://digitalcommons.usu.edu/etd>

 Part of the [Physics Commons](#)

Recommended Citation

Wood, Brian D., "Optical Characterization of Carbon Nanotube Forests" (2015). *All Graduate Theses and Dissertations*. 4567.

<https://digitalcommons.usu.edu/etd/4567>

This Thesis is brought to you for free and open access by the Graduate Studies at DigitalCommons@USU. It has been accepted for inclusion in All Graduate Theses and Dissertations by an authorized administrator of DigitalCommons@USU. For more information, please contact digitalcommons@usu.edu.



OPTICAL CHARACTERIZATION OF CARBON

NANOTUBE FORESTS

by

Brian D. Wood

A thesis submitted in partial fulfillment
of the requirements for the degree

of

MASTER OF SCIENCE

in

Physics

Approved:

Dr. T.C. Shen
Major Professor

Dr. D. M. Riffe
Committee Member

Dr. James Dyer
Committee Member

Dr. Mark R. McLellan
Vice President for Research and
Dean of the School of Graduate Studies

UTAH STATE UNIVERSITY
Logan, Utah

2015

Copyright © Brian D. Wood 2015

All Rights Reserved

ABSTRACT

Optical Characterization of Carbon Nanotube Forests

by

Brian D. Wood, Master of Science

Utah State University, 2015

Major Professor: Dr. T.C. Shen
Department: Physics

Carbon nanotube forests are vertically grown tubular formations of graphene. Samples were grown with an injection chemical vapor deposition method on substrates of silicon with various deposited layers and bare fused silica. The morphology of the forest is characterized by the height, density, and presence of defects. Total diffuse reflectance and transmittance measurements were taken in the 2-16 μm spectral range and correlated to the forest's specific morphology. From these correlations, the conditions necessary to maximize the absorption of the forest were found and exploited to cater sample growth for specific substrates to make ideal absorbers. From the transmittance data, the absorption coefficient is found via Beer-Lambert's Law and also correlated to sample morphology, giving us an indication of the height of the forest needed for ideal absorption. Two models were used to attempt to reproduce the experimental absorption coefficient: an effective medium theory using a Maxwell Garnett approximation and by treating the carbon nanotube forest as an effective cylindrical waveguide with walls of

graphite. Each model leads to a set of fitting parameters providing a better physical understanding of the forests. It was found that the effective medium theory gave results loosely corroborated with electron microscopy, but had trouble fitting the experimental data, and the index of refraction it provides does not behave like a unified medium. The waveguide model fits the data well, but it requires more experimental evidence to be more conclusive. The theoretical models need more work, but fabrication of ideal absorbers has been achieved on various substrates providing framework for their usage in radiometry and spectroscopy.

(82 Pages)

PUBLIC ABSTRACT

Optical Characterization of Carbon Nanotube Forests

Brian D. Wood

Carbon nanotube forests are vertically grown tubular formations of graphene. Due to their inherent microstructure and geometry, they are ideal light absorbers over a broad spectrum, making this material an excellent absorber in applications such as radiometry, optical calibration, and stray light suppression. Samples were made with several growth conditions and substrates to provide forests of different morphologies. Optical data of these samples were gathered by taking spectroscopic reflectance and transmittance measurements in the mid-infrared spectral range. Results were correlated to the various forest morphologies. From this, the conditions necessary to maximize the absorption of the forests were found and can be used to cater nanotube growth for specific substrates and applications. The absorption of these samples is characterized by an absorption coefficient that is extracted from the transmittance data. Two mathematical models were used to reproduce the forest's absorption data. Relevant physical attributes can be gathered from these models and corroborated with scanning electron microscopy to provide a better understanding of the optical properties of carbon nanotubes.

ACKNOWLEDGMENTS

I would like to thank my mentor, Dr. T.C. Shen, for providing both the insight into this project, along with the commitment and guidance he has given me along its course. My committee members, Dr. Mark Riffe and Dr. James Dyer, deserve thanks for their advice and encouragement along the way of my program. Thanks go to the USU College of Science, Department of Physics, and School of Graduate Studies for their corrections and support, and finally, Space Dynamics Lab and the Utah NASA EPSCoR Research Student Opportunity for providing funding for the project.

Brian D. Wood

CONTENTS

	Page
ABSTRACT.....	iii
PUBLIC ABSTRACT	v
ACKNOWLEDGMENTS	vi
LIST OF TABLES	ix
LIST OF FIGURES	x
INTRODUCTION	1
THEORY	3
Thin Film Optics	3
Effective Medium Theory	9
Waveguide Model	16
PROCEDURE.....	19
Sample Growth.....	19
Data Acquisition.....	21
Reflectance	23
Transmittance	31
RESULTS	32
Substrates	33
Carbon Nanotube Forests	35
Aluminum/Silicon Samples.....	35
Quartz Samples.....	39
Niobium/Aluminum/Silicon Samples.....	42
Absorption Coefficient and Skin Depth.....	45
Aluminum/Silicon Samples.....	46
Quartz Samples.....	49

Effective Medium Theory	50
Aluminum/Silicon Samples	52
Quartz Samples	55
Waveguide Model	56
Aluminum/Silicon Samples	58
Quartz Samples	60
CONCLUSIONS.....	62
REFERENCES	65
APPENDIX.....	67

LIST OF TABLES

Table		Page
I	List of growth parameters affecting the morphology and defect level.....	21
II	Ferrocene concentration and height of the five samples grown on Al/Si.....	35
III	Ferrocene concentration and height of three CNT forest samples grown on quartz	40
IV	Ferrocene concentration and heights of four samples grown on Al/Nb	43
V	Table of T values for various distances, d.....	48
VI	EMT parameters for Al/Si 127-Al/Si 133	54
VII	EMT parameters for Q 125 and Q 134	56
VIII	Waveguide parameters for Al/Si 127-Al/Si 133.....	60
IX	Waveguide parameters for Q 125 and Q 134	61

LIST OF FIGURES

Figure	Page
1	Dissected reflection components of incident intensity 3
2	Schematic of optical path difference between both reflected rays 6
3	Transmission coefficients of sample and substrate transmitted intensity..... 7
4	The \hat{c} axis of the graphene sheet and the dielectric components referenced to it.. 10
5	General ellipsoid showing semi-axis (x,y,z) and their respective depolarization values 13
6	Example of an effective radius for a certain point within the CNT forest 16
7	Schematic of growth setup 19
8	Bare background signal of the integrating sphere 23
9	Schematic of (a) sample, and (b) reference positions of the integrating sphere showing the two components of incoming radiation..... 24
10	Graph showing the reflectance data taken with and without the subtraction factor of the 2% standard compared with the data provided by Avian 28
11	Graph comparing the standard data to ours taken with various aperture sizes in the spectrometer..... 29
12	Data taken on Al/Si 127 B2 with various aperture sizes of the spectrometer 30
13	Schematic showing the (a) sample, and (b) reference positions for transmittance data acquisition 31
14	Schematic of reflection components..... 32
15	Reflectance of the three substrates used for sample growth..... 34
16	Transmittance of the three substrates used for sample growth..... 35
17	Reflectance of lower density forests Al/Si 132 and Al/Si 133 36

Figure	Page
18	Reflectance of Al/Si 127, Al/Si 129, and Al/Si 124..... 37
19	Transmittance of all Al/Si samples except Al/Si 124 due to its near zero values . 38
20	Reflectance for samples Q 125, Q 130, and Q 134 40
21	Transmittance of samples Q 125 and Q 134..... 41
22	Transmittance of all quartz samples focusing on the region of 5 μm 42
23	Reflectance of the denser Al/Nb samples of 0.5% ferrocene concentration, but with different heights..... 44
24	Reflectance of the less dense Al/Nb samples of 0.2% ferrocene concentration, but with different heights..... 44
25	Plot showing the absorption coefficient for the Al/Si samples 46
26	Plot showing the skin depth for the Al/Si samples 48
27	Plot showing the absorption coefficient for the quartz samples 49
28	Plot showing the skin depth of the quartz samples..... 50
29	Figure of electric field orientations and their designated polarizations..... 51
30	Absorption coefficient of Al/Si 127 graphed with two EMT model curves 52
31	Absorption coefficient of Al/Si 129 graphed with two EMT model curves 53
32	Absorption coefficient of Al/Si 132 graphed with two EMT model curves 53
33	Absorption coefficient of Al/Si 133 graphed with two EMT model curves 54
34	Absorption coefficient of Q 125 graphed with two EMT model curves 55
35	Absorption coefficient of Q 134 graphed with two EMT model curves 56
36	Absorption coefficient of Al/Si 127 graphed with the waveguide model curve ... 58
37	Absorption coefficient of Al/Si 129 graphed with the waveguide model curve ... 58

Figure	Page
38	Absorption coefficient of Al/Si 132 graphed with the waveguide model curve ... 59
39	Absorption coefficient of Al/Si 133 graphed with the waveguide model curve ... 59
40	Absorption coefficient of Q 125 graphed with the waveguide model curve..... 61
41	Absorption coefficient of Q 134 graphed with the waveguide model curve..... 61
A.1	SEM images of samples of similar height of 25 microns, but different ferrocene concentration, a) Al/Si 127 base/side view, b) top view visibly more dense than c) Al/Si 132 base/side view, and d) top view 68
A.2	SEM images of samples with similar height around 45 microns, but different ferrocene concentrations 69
A.3	Highly dense sample Al/Si 124 a) base/side view showing catalyst particle defects, and b) top view showing entanglement..... 69
A.4	Base, side views comparing the denser a) Q 125 with b) Q 130..... 70
A.5	Displaying top surface corrugation on successively different scales of a) Al/Nb 126, scale bar 1.2 μm , b) Al/Nb 135, scale bar 3.75 μm , c) Al/Nb 131, scale bar 20 μm , and a side view of d) Al/Nb 126, scale bar 7.5 μm 70

INTRODUCTION

This thesis is an in-depth study of the optical characterization of carbon nanotube (CNT) forests grown on substrates of silicon and quartz. Discussion starts with the growth procedure, which involves a chemical vapor deposition (CVD) method. Several CNT forest samples were grown on various substrates while varying the growth conditions. By investigating the total reflectance and transmittance of these different samples, we attempted to decipher how the growth conditions and defects affect the optical properties. Optical data were gathered using a Fourier transform infrared spectrometer (FTIR) with an integrating sphere accessory. The absorption coefficient is then extracted by using the Beer-Lambert law^{1,2} with the transmittance data. Two models are then used to attempt recreation of these coefficients. Effective Medium Theory (EMT) is an approach used to describe the dielectric response of inhomogeneous materials by weighing the polarization of cylindrical inclusions within a host medium. The other model treats the forest as an effective cylindrical waveguide composed of walls of graphite with absorption due to its finite conductivity. These models are used to fit the experimental data as close as possible, of which their results are compared, and the physical relevance of their fitting parameters is discussed.

The optical characterization of carbon nanotubes has been studied by several groups; however, due to the inherent optical anisotropy of CNT films, there are variations in the reported data^{1,3-9}. Most of these groups have similar low-end values for the reflectance in the mid-IR spectrum, but the results vary with increasing wavelength. These differences arise from such issues as angle of incidence, morphology of their structure dictated by their density, height, chirality and absence of defects, wavelengths

of interest, growth method, and substrates. Since the reflectance of these CNTs are so low, instrument type and precision plays a role in the presented values of these groups, as well. The optical absorption of graphene has been studied for some time. Since CNTs are a tubular formation of graphene, this can be extended to the mechanism of the absorption of the CNT forest. Graphene itself acts as an absorber through a broad wavelength range¹⁰ due to both interband and intraband optical absorption depending on the energy of incoming radiation. The difference between graphene and a CNT forest being, of course, the geometry of the graphite layers. The low reflectivity of the forest top is believed to be due to a near unity refractive index, hence reducing the air to CNT boundary. It has also been shown a gradient-index surface of many materials can greatly reduce the reflectance of that surface¹¹. This effect not only conveys the radiation to the silicon substrate, but can reduce the reflectance of the CNT forest top because the forest may have height variations, allowing a secondary refractive index transition. Once a photon has breached the reflective interface, there is a great probability to be absorbed in the forest from the multiple reflections and optical band transitions within the graphene structure of the tubes. From a device point of view, the total reflectance and transmission of the sample including the substrate is the pertinent data to be analyzing. By normalizing the transmittance data with that of a bare substrate annealed at the same growth temperature, study of solely the vertically aligned CNT forest can be carried out without the substrate contribution, which is used for the absorption coefficient analysis.

THEORY

Thin Film Optics

Analyzing the optical data of our carbon nanotubes was a difficult task. Since our forest's heights range from 20-110 μm tall, they are treated as a thin film medium that is highly absorptive and inhomogeneous throughout their height. Thin film optical phenomena has been understood for quite some time, and we have been able to extend this to the study. There are, in theory, infinite orders of reflectance as a result of the multiple internal reflections within the medium emerging. However, the amplitude of the first two orders derived from the Fresnel relations for even a nonabsorbent medium are more than two orders of magnitude greater than the third's reflected intensity². Therefore, the total reflectance of the sample, i.e., the radiation received by the detector is dissected into two components, shown in Fig. 1. Each component is a portion of the incident intensity characterized with optical factors. These factors are similar to the Fresnel amplitude coefficients, but are wavelength dependent, and polarization is not considered.

The factors ρ and τ are the fraction of intensity that is reflected and transmitted at an interface, respectively, where τ is defined as $(1 - \rho)$. The first reflected component is that off of the top, or crust of the sample designated I_1 , which is simply

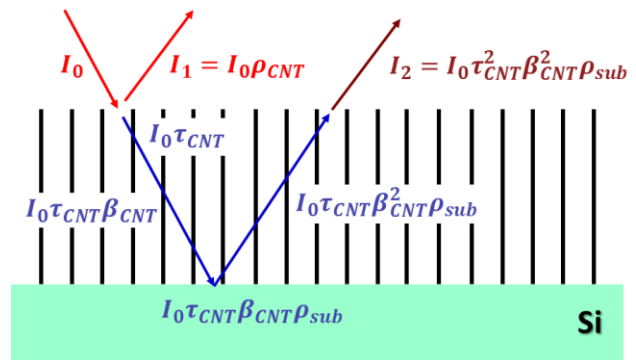


FIG. 1. Dissected reflection components of incident intensity.

equal to the product of the incident intensity with the crust's reflectance. A portion will also penetrate into the forest receiving a transmittance factor, τ_{CNT} , and travel through the CNT forest. As it travels, it will get attenuated by the forest, represented with the β_{CNT} term. Since the CNT forest is not homogeneous, β_{CNT} technically should be a quantity dependent on height, $\beta_{CNT}(h)$. However, since the factor is only considered after it has traveled through the entire substrate, we remove this dependence and consider it an integrated quantity. The wave then reflects off of the substrate whose surface reflectance is labeled as ρ_{sub} . This reflectance has a possibility to be slightly different than the reflectance of a bare annealed substrate, since there are catalyst particles embedded in the surface. As the wave goes back up through the forest, it picks up another attenuation factor, along with another transmittance factor, τ_{CNT} , as it escapes the forest. Again, approximation has been taken into account for whether the transmission factor going in is the same as it is escaping the forest, i.e., this factor is independent on the wave's direction. The detector of the integrating sphere will pick up the total escaping intensity, which is a combination of I_1 and I_2 .

$$R_{sample} = I_1 + I_2 = I_o(\rho_{CNT} + \tau_{CNT}^2 \beta_{CNT}^2 \rho_{sub}). \quad (2.1.1)$$

If the forest is absorbent enough, the β_{CNT}^2 term will attenuate the substrate reflection so I_1 will be the primary intensity collected by the detector. If, however, the refracted wave makes it out of the forest, two things can happen: (1) the reflectance data will exhibit features characteristic of the substrate contained in the ρ_{sub} term, or (2) I_2 will have an opportunity to interfere with the primary reflected wave, I_1 .

Interference between two waves that are parallel to each other can be treated as

the scalar addition of the two intensities along with a contributing interference term shown as

$$I_{Tot} = I_1 + I_2 + 2\sqrt{I_1 I_2} \cos(k_0 \Lambda), \quad (2.1.2)$$

where k_0 is the wave number in free space and Λ is the optical path difference between the two waves defined as¹¹

$$\Lambda = n_{cnt}(\overline{AB} + \overline{BC}) - n_{air}(\overline{AD}). \quad (2.1.3)$$

Using the geometry of a thin film, as shown in Fig. 2, the optical path difference can be simplified to

$$\Lambda = 2dn_{cnt} \cos \theta_t, \quad (2.1.4)$$

where d is the height of the forest, n_{cnt} is the index of refraction of the forest, and θ_t is the transmitted angle. $\cos \theta_t$ is very close to one, due to the experimental incident angle being 8° , even using the highest projected values of n_{CNT} given by both theoretical and experimental results of others^{1,3,4,8}. Therefore, the total reflectance defined as $\frac{I_{tot}}{I_0}$, can now be written as

$$R_{Tot} = \left[\rho_{CNT} + \tau_{CNT}^2 \beta_{CNT}^2 \rho_{sub} + 2\tau_{CNT} \beta_{CNT} \sqrt{\rho_{CNT} \rho_{sub}} \cos\left(\frac{4\pi d n_{cnt}}{\lambda}\right) \right]. \quad (2.1.5)$$

This equation, in conjunction with one derived from the transmission data, can derive the index of refraction of the forest as a function of wavelength.

If the reflectance from the sample is negligible, the normalized transmittance can be written as

$$T_{sample} = \tau_{CNT} \beta_{CNT} \beta_{Si} \tau_{sub}^2, \quad (2.1.6)$$

as seen in Fig. 3. It contains attenuation coefficients of both the CNT forest and the silicon substrate. From a device standpoint, the relevant data will be that of the whole sample including both the CNT forest and the substrate since we want all of the radiation to be absorbed into either of these media. I also

investigated the transmittance of just the

CNT forest without the substrate contribution. This is accomplished by taking transmittance data of a bare substrate annealed in the same ambient gas and temperature as in CNT growth and then dividing the entire sample data to that of the substrate's.

Using $T_{Substrate} = \beta_{Si} \tau_{sub}^2$ as the collected transmitted intensity of the substrate, this yields

$$T_{CNT} = \tau_{CNT} \beta_{CNT}. \quad (2.1.7)$$

This expression can also be inserted into Eq. (2.1.6) to get

$$R_{CNT}(\lambda) = \left[\rho_{CNT} + T_{CNT}^2 \rho_{sub} + 2T_{CNT} \sqrt{\rho_{CNT} \rho_{sub}} \cos\left(\frac{4\pi d n_{cnt}}{\lambda}\right) \right]. \quad (2.1.8)$$

The known factors in this expression would include the data T_{CNT} and ρ_{sub} collected from the integrating sphere, along with the height, d , of the forest found through scanning

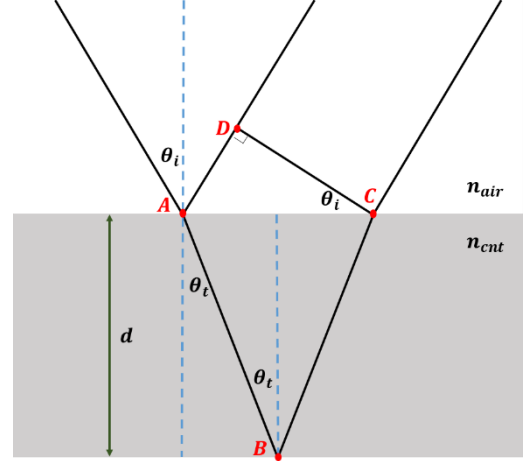


FIG. 2. Schematic of optical path difference between both reflected rays.

electron microscope (SEM) images.

ρ_{CNT} and n_{CNT} can be modeled with a multivariable function with its parameters tweaked to match the total reflectance data. Once satisfactory fitting of the data has been achieved, we now have the reflectance and the effective refractive index of a CNT forest as functions of wavelength.

Application of the Beer-Lambert law¹ to the CNT forests allows us to deduce the absorption coefficient of the forest. The law is mainly used for light traveling through gaseous and dilute liquid chemical solutions. Since most of the space in a CNT forest is empty, the Beer-Lambert law may be applicable. The law states the change in light intensity is proportional to the traveling intensity and the distance the light travels. This is written differentially as¹²

$$dI = -\alpha \cdot I \cdot dz. \quad (2.1.9)$$

Solving Eq. (2.1.9), the intensity of the light into the forest can be written as

$$I = I_0 e^{-\alpha \cdot d}, \quad (2.1.10)$$

where I_0 is the incident intensity, α is the absorption coefficient and d is the height of the forest. The measured quantity, the transmittance, is a normalized quantity to the incident

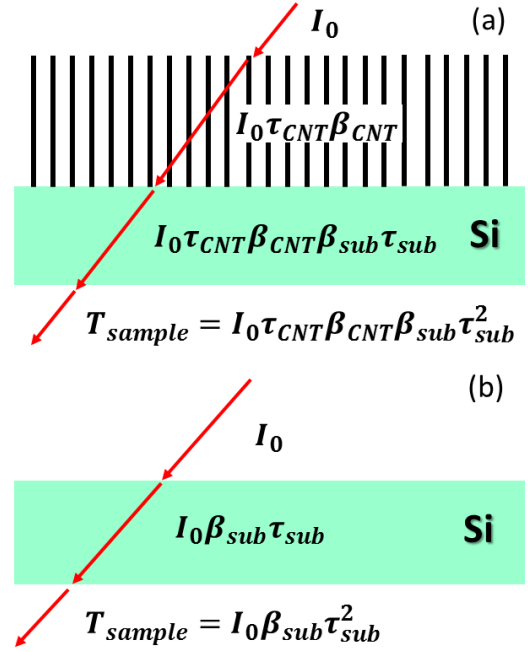


FIG. 3. Transmission coefficients of sample and substrate transmitted intensity.

intensity

$$T_{sample} = \frac{I_{sample}}{I_0} = e^{-a \cdot d}, \quad (2.1.11)$$

where I_{sample} and I_0 are individual data runs taken from the spectrometer. As discussed above, the transmittance of the CNT forest can be obtained by dividing out the bare substrate transmittance from the sample transmittance. The absorption coefficient of the CNT forest is now solved for as¹

$$\alpha = -\frac{1}{d} \ln \left(\frac{T_{sample}}{T_{substrate}} \right). \quad (2.1.12)$$

From this result, we can relate the absorption coefficient to the density and height of the specific forests.

Through SEM imaging, however, it has been shown the density of the forest is not constant throughout its height¹³. Therefore, the absorption coefficient α would be a function of the height. If we assume a linear relationship, α can be written as

$$\alpha(z) = m \cdot z, \quad (2.1.13)$$

where m describes the rate of change of density throughout the height dictated by growth.

The differential equation is now

$$\frac{dI}{I} = -(m \cdot z) \cdot dz. \quad (2.1.14)$$

When solved, this yields

$$I = I_0 e^{-\frac{1}{2} m d^2}. \quad (2.1.15)$$

The absorption coefficient and m are simply related by

$$\alpha = \frac{1}{2}md. \quad (2.1.16)$$

To summarize, the reflectance data collected will be primarily contributed from the reflectance of the top crust of the forest. If the forest has a low enough CNT density, then there is a possibility of the substrate contributing to the reflectance data. Comparing this to reflectance data of a bare annealed substrate allows us to determine which features may have been contributed by the substrate. We can also remove the substrate contribution from the transmittance data by normalizing the transmittance of the whole sample to that of the annealed substrate. If the sample is diluted even more, interference fringes can be observed. Using a multivariable reflectance model along with reflectance and transmittance data, we can investigate the absorption coefficient and the effective refractive index of a forest.

Effective Medium Theory

Effective medium theory or effective medium approximations have been used successfully to characterize the dielectric properties of inhomogeneous materials. The Maxwell Garnett (MG) approximation is essentially a Clausius-Mossotti relation modified for cylindrical geometry with a depolarization field contribution. It consists of a mixing formulation using dielectric contributions of inclusions within a host medium, weighted with a filling factor.^{8,14,15} The basis of this formulation uses both dielectric functions of bulk graphite's dielectric, ϵ_{\perp} and ϵ_{\parallel} . This yields an effective dielectric of the carbon nanotube forest that will depend on the polarization of incoming radiation; the contributions of each are then portioned with an alignment factor^{1,8} of the CNT forest to

give a total effective dielectric function. Once this is obtained, the absorption coefficient is extracted and parameters are modified to fit the experimental data.

Multiwalled carbon nanotubes are considered to be a tubular formation of graphene sheets, thus the walls of a CNT can be approximated as bulk graphite. Vidal *et al.*^{8,14,15} have investigated hollow tube effects on the dielectric and discovered it is safe to ignore the hollow core when considering CNT bundles and when the outer radius is roughly twice that of the inner one¹⁴. This study uses the dielectric of graphite compiled by Draine and Lee for the MG formulation.¹⁶ Graphite is a highly anisotropic material, responding differently to different polarizations of radiation. Defining a \hat{c} axis normal to the basal plane of graphite references the dielectric components ϵ_{\perp} and ϵ_{\parallel} as seen in Fig. 4. Each component takes the form of¹⁶

$$\epsilon_{\perp,\parallel} = 1 + \delta\epsilon^b + \delta\epsilon^f = \epsilon_1 + i\epsilon_2, \quad (2.2.1)$$

where $\delta\epsilon^b$ is the bound or interband contribution and $\delta\epsilon^f$ is the free or intraband contribution; each of which consist of real and imaginary parts. The intraband contribution is approximated with a free-electron Drude model for both the parallel and perpendicular components, given as

$$-\frac{(\omega_p\tau)^2}{(\omega\tau)^2 + i\omega\tau} = Re(\delta\epsilon^f) + i \cdot Im(\delta\epsilon^f), \quad (2.2.2)$$

where ω_p is the plasma frequency and τ is the mean collision time between electrons and nuclei that has been found

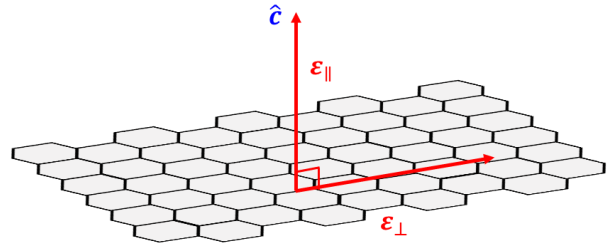


FIG. 4. The \hat{c} axis of the graphene sheet and the dielectric components referenced to it.

experimentally. An iterative method is used to find the interband contribution. This is done by first measuring and choosing the imaginary part of total dielectric, $\epsilon_{\perp,\parallel}$. The difference is then taken with the imaginary component of the free-electron contribution to give the imaginary component of the bound term,

$$Im(1 + \delta\epsilon^b) = [Im(\epsilon_{\perp,\parallel}) - Im(\delta\epsilon^f)]. \quad (2.2.3)$$

The Kramers-Kronig relation mathematically correlates the real part of an analytic function to its imaginary counterpart. Physically, it relates the dispersive and absorptive properties of a medium and is commonly used in dielectric analysis. In this case, the Kramers-Kronig relation is given as

$$\epsilon_1(\omega) = 1 + \frac{2}{\pi} P \int_0^{\infty} \frac{\omega' \epsilon_2(\omega')}{\omega'^2 - \omega^2} d\omega', \quad (2.2.4)$$

where P is the principal value of the integral. When available, $\epsilon_1(\omega)$ was compared to experimental data and adjustments to the frequency or chosen $\epsilon_2(\omega)$ were done if necessary. This process was repeated until acceptable data of the real and imaginary parts of both polarizations was acquired. Draine and Lee¹⁶ have acquired this data over a broad wavelength range, but we only capitalize on the mid-IR spectrum used in the MG approximation.

Garcia-Vidal *et al.* have extensively studied and characterized CNT films by two methods.^{8,14,15} One method used to find the dielectric function of the forest uses a perturbative, or on-shell method to find the dielectric. This is done by finding solutions to Maxwell's equations with a tensor dielectric that will satisfy a Bloch wave dispersion relation. This method is entirely numerical and is outlined in detail in Refs. [17], [18],

and [19]. The MG method is an approximation of this result that is the main use in this study, utilizing the dielectric function of graphene outlined above. The Maxwell-Garnett (MG) approach assumes a low concentration of constituents and approximates the field inside and outside the particles to be homogeneous. The derivation follows from Lü²⁰ that defines the effective dielectric of the compound as the ratio of the average displacement field to that of the average electric field. The average electric and displacement field is given as a fraction of the field from each constituent²⁰

$$\vec{E}_{ave} = f\vec{E}_1 + (1-f)\vec{E}_2 = f\vec{E}_0 + (1-f)\vec{E}_{cnt}, \quad (2.2.5)$$

$$\vec{D}_{ave} = f\varepsilon_o\varepsilon_1\vec{E}_1 + (1-f)\varepsilon_o\varepsilon_2\vec{E}_2 = f\varepsilon_o\vec{E}_0 + (1-f)\varepsilon_o\varepsilon_{cnt}\vec{E}_{cnt}, \quad (2.2.6)$$

where f is a filling factor or volume fraction occupied, ε_1 and ε_2 are the relative permittivities of component 1 and 2, respectively, and \vec{E}_1 and \vec{E}_2 are the electric fields within that constituent. The last steps use notation appropriate for a CNT forest, where $\vec{E}_1 = \vec{E}_0$ is the external field and $\vec{E}_2 = \vec{E}_{cnt}$ is the field within the carbon nanotube, while $\varepsilon_1 = 1$ for air and $\varepsilon_2 = \varepsilon_{cnt}$. The electric field in air will only be the external field from the radiation, ignoring the perturbing field from the induced polarization of nearby atoms in a nanotube, while the field within the nanotube will be only the field generated from each atom being polarized by the external field, again following the MG approximation. Considering a general ellipsoid, the polarization field inside the particle in terms of the external field is given as²¹

$$\vec{E}_2 = \frac{\varepsilon_1}{\varepsilon_1 + L(\varepsilon_2 - \varepsilon_1)}\vec{E}_1 \Rightarrow \vec{E}_{cnt} = \frac{1}{1 + L(\varepsilon_{cnt} - 1)}\vec{E}_0, \quad (2.2.7)$$

using the forest notation in the final step and L is a geometrical, or depolarization factor,

depending upon which semi axis the field is being directed along the ellipsoid. A carbon nanotube is considered to be a needle, which is the limiting case when the diameter is much smaller than the length of the ellipsoid, giving the depolarization factors $(\frac{1}{2}, \frac{1}{2}, 0)$ as shown in Fig. 5. Stated earlier, the effective dielectric of the mixture is²⁰

$$\epsilon_{eff} = \frac{\vec{D}_{ave}}{\epsilon_0 \vec{E}_{ave}}. \quad (2.2.8)$$

Using equations (2.2.5-2.2.7) with this ratio will yield

$$\begin{aligned} \epsilon_{eff} &= \epsilon_1 + \frac{f \epsilon_1 (\epsilon_2 - \epsilon_1)}{\epsilon_1 + L(\epsilon_2 - \epsilon_1) - fL(\epsilon_2 - \epsilon_1)} \\ &= 1 + \frac{f(\epsilon_{cnt} - 1)}{1 + L(\epsilon_{cnt} - 1) - fL(\epsilon_{cnt} - 1)}, \end{aligned} \quad (2.2.9)$$

where again the last line uses the notation appropriate for the forest. Due to the inherent anisotropy of graphene, this is emulated in the CNT forest and the polarization of incoming radiation needs to be considered to determine what to use for ϵ_{cnt} . s-polarization is defined as having the electric field directed along the length of the nanotube while p-polarization as directed perpendicular to this axis. For s-polarization, the dielectric of the carbon nanotube, $\epsilon_{cnt}^s = \epsilon_{\perp}$, the perpendicular dielectric function of graphene, as the

radiation only sees
the tube as a
homogeneous
medium from this
direction. Along the

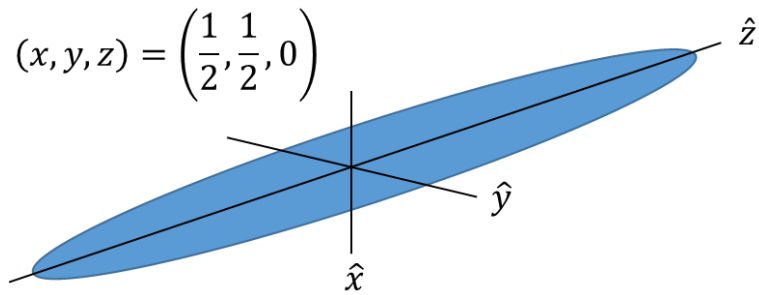


FIG. 5. General ellipsoid showing semi-axis (x,y,z) and their respective depolarization values.

length of the tube, the depolarization factor $L = 0$ and equation (2.2.9) becomes

$$\varepsilon_{eff}^s(\omega) = f\varepsilon_{\perp}(\omega) + 1 - f. \quad (2.2.10)$$

For p-polarization, ε_{\parallel} cannot simply be used due to edge effects in this direction. This issue is resolved by considering the atomic polarizability of a carbon nanotube, given as²²

$$\alpha_m = 4\pi\varepsilon_0\varepsilon_e R^{2m} \frac{(\varepsilon_{\parallel}\lambda - \varepsilon_i)(\varepsilon_{\parallel}\lambda + \varepsilon_e)\rho^{2m'} - (\varepsilon_{\parallel}\lambda - \varepsilon_e)(\varepsilon_{\parallel}\lambda + \varepsilon_i)}{(\varepsilon_{\parallel}\lambda - \varepsilon_i)(\varepsilon_{\parallel}\lambda - \varepsilon_e)\rho^{2m'} - (\varepsilon_{\parallel}\lambda + \varepsilon_e)(\varepsilon_{\parallel}\lambda + \varepsilon_i)}, \quad (2.2.11)$$

where ε_i and ε_e are the relative dielectric functions of the internal and external

composites, $\rho = \frac{r}{R}$, the ratio of the inner and outer radii of the nanotube, $m' = m\sqrt{\frac{\varepsilon_{\perp}}{\varepsilon_{\parallel}}}$ and

$\lambda = \frac{m'}{m}$. Ref [21] has proposed creating an isotropic dielectric function for a nanotube by

letting $\varepsilon_{\parallel} = \varepsilon_{\perp} = \varepsilon$ in (2.2.11). Calling this function's polarizability, α'_m , and equating it

to α_m provides an equivalent isotropic dielectric function for an anisotropic carbon

nanotube. Assuming the outer radius is much larger than the inner then $\rho \approx 0$ and $\varepsilon =$

$\varepsilon_{cnt}^p = \sqrt{\varepsilon_{\perp}\varepsilon_{\parallel}}$. Along the x and y directions, $L = \frac{1}{2}$ and equation (2.2.9) becomes

$$\varepsilon_{eff}^p(\omega) = \frac{\sqrt{\varepsilon_{\parallel}(\omega)\varepsilon_{\perp}(\omega)}(1 + f) + 1 - f}{\sqrt{\varepsilon_{\parallel}(\omega)\varepsilon_{\perp}(\omega)}(1 - f) + 1 + f}. \quad (2.2.12)$$

Equations (2.2.10) and (2.2.12) constitute the dielectric functions for an array of carbon

nanotubes for the electric field oriented parallel and perpendicular to the nanotubes,

respectively. The contribution from these components is portioned with an alignment

factor, X , defined as the contribution of the dielectric function within s-polarization, to

give the total effective dielectric of the CNT film as^{1,8}

$$\varepsilon_{eff}^{tot} = X\varepsilon_{eff}^p(\omega) + (1 - X)\varepsilon_{eff}^s(\omega). \quad (2.2.13)$$

With the effective dielectric constant now attained, its real and imaginary parts are now related to the complex index of refraction, $\tilde{n} = n + i\kappa$ via

$$\varepsilon_{eff} = (\varepsilon_1 + i\varepsilon_2)_{eff} = (n + i\kappa)^2. \quad (2.2.14)$$

n is the real part of the index of refraction, and κ is referred to as the attenuation constant as it is responsible for the radiation loss in a medium. This can be seen by inserting the complex wave number, $\tilde{k} = \frac{2\pi}{\lambda_0} \tilde{n}$, into the plane wave solution

$$\begin{aligned} \tilde{\mathbf{E}}(z, t) &= \tilde{\mathbf{E}}_0 e^{i(\tilde{k}z - \omega t)} = \tilde{\mathbf{E}}_0 e^{i\left[\frac{2\pi(n+i\kappa)}{\lambda}z - \omega t\right]} \\ &= \tilde{\mathbf{E}}_0 e^{-\frac{2\pi\kappa}{\lambda}z} e^{i\left(\frac{2\pi n}{\lambda}z - \omega t\right)}. \end{aligned} \quad (2.2.15)$$

The field amplitude now drops off as $e^{-\frac{2\pi\kappa}{\lambda}z}$. Recalling the Beer-Lambert law relates the absorption coefficient with the drop of intensity by

$$I(z) = I_0 e^{-\alpha z}, \quad (2.2.16)$$

and since the intensity of radiation is proportional to the square of the E field, the absorption coefficient as a function of wavelength is now²

$$\alpha(\lambda) = \frac{4\pi\kappa}{\lambda}. \quad (2.2.17)$$

κ is now found using the real and imaginary parts of the effective dielectric

$$\kappa = \sqrt{\frac{\sqrt{\varepsilon_1^2 + \varepsilon_2^2} - \varepsilon_1}{2}}. \quad (2.2.18)$$

ε_1 and ε_2 are the real and imaginary parts of the effective dielectric function, respectively, of a CNT forest, whose graphite components are given as a function of

wavelength¹⁶. Using equations (2.2.17) and (2.2.18) in conjunction with the Draine and Lee data has now given the Maxwell-Garnett approach to modeling the absorption coefficient of the CNT forest with the fitting parameters, f , the filling fraction, and X , the forest alignment factor.

Waveguide Model

Electromagnetic energy dissipation can be considered as an ohmic loss along a transmitting waveguide due to its finite conductivity. A CNT forest physically is far from a waveguide, however, by treating the EM radiation impinging on a CNT forest as having the same boundary conditions as those on a cylindrical waveguide composed of graphite has given satisfactory results. Considering a single point in the forest bombarded by radiation, the waves will interact with local nanotubes as it propagates downward.

Considering a single point in the forest, the E field of a single wave of a given

polarization will interact with the two

nearest nanotube neighbors. Depending on

the distance between these tubes dictates

whether the wave will propagate or be

attenuated. This will happen many times

over in every direction, generating an

effective radius of a waveguide at this point

as seen in Fig. 6. Morphology and density of

the forest dictates the radius of the

waveguide. Modifications of typical

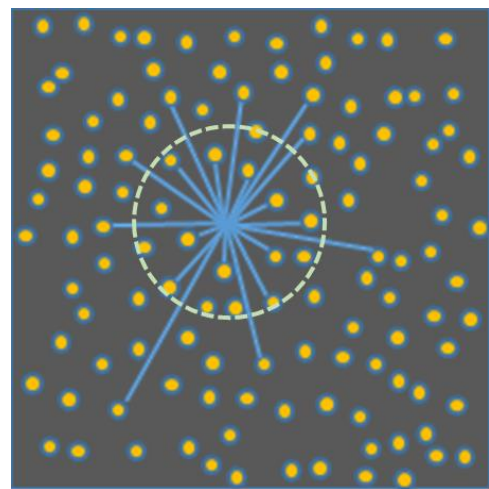


FIG. 6. Example of an effective radius for a certain point within the CNT forest.

transmission theory to accommodate modeling a CNT forest include incorporation of the anisotropy of graphite's dielectric along with a general conductivity reduction factor, S_o . The reduced conductivity as a function of graphite's frequency-dependent dielectric function is²³

$$\sigma(\omega) = \frac{-i\omega\varepsilon_0[\varepsilon(\omega) - 1]}{S_o}. \quad (2.3.1)$$

As mentioned before, the components of the complex dielectric of graphite are separated into two components, parallel and perpendicular to the c-axis. Similar to Ye *et al.*¹, the contribution of these components is weighted with an alignment factor,

$$\varepsilon(\omega) = X\varepsilon_{\perp} + (1 - X)\varepsilon_{\parallel}, \quad (2.3.2)$$

where ε_{\perp} and ε_{\parallel} are the dielectric functions of graphite as defined in Eq. (2.2.1).

Attenuation of energy due to metallic loss is found by the dissipation of power per unit length. Power flow along a waveguide is given by²⁴

$$P(z) = P_0 e^{-2\alpha z}, \quad (2.3.3)$$

where P_0 is the power along a lossless line, and α is the absorption coefficient, that when solved for gives

$$\alpha = \frac{-1}{2P_0} \frac{dP}{dz}. \quad (2.3.4)$$

P_0 is the time-averaged Poynting vector. By applying appropriate boundary conditions for cylindrical geometry, the absorption coefficient of the waveguide can be written as²⁴

$$\alpha = \frac{2}{ak\eta\sigma_R(\omega)\delta\sqrt{k^2 - k_c^2}} \left[k_c^2 + \frac{k^2}{p_{nm}^2 - 1} \right], \quad (2.3.5)$$

where a is the effective radius of the waveguide, k is the wavenumber, η is the vacuum impedance, $\sigma_R(\omega)$ is the real part of the conductivity, δ the skin depth, and finally the cutoff wavenumber, $k_c = \frac{p_{nm}}{a}$, where p_{nm} is the m^{th} derivative of the Bessel function, J'_n . This model now has three fitting parameters: the alignment factor, X , the conductivity reduction factor, S_o , and the effective radius, a , to match the experimental data.

PROCEDURE

Sample Growth

Several methods for growing carbon nanotubes exist; the first being implemented in 1991 by Iijima²⁵ was an arc discharge method. Laser ablation, and then finally, the preferred method of chemical vapor deposition (CVD) was established. Arc discharge easily fabricates single and multiwalled carbon nanotubes of fair purity²⁶. Laser ablation was undertaken soon afterward, and can produce very pure SWCNT's²⁷. These methods, however, produce nanotubes that are parallel to the supporting structure. The desired structure of the CNTs is vertically grown on the substrate, as this drastically increases the light absorption of the film. A viable process for creating a large array of highly aligned carbon nanotubes was reported by Z. F. Ren²⁸ *et al.* in 1996 using a CVD method on silica substrates. We have grown our samples on several substrates using a nonplasma-enhanced CVD method. Fig. 7 shows a schematic of our growth system setup. To start, the substrate is loaded

into the tube furnace and brought up to temperature, which for this study, 700 °C was found to be the ideal temperature. A chemical precursor consisting of a ferrocene [$\text{Fe}(\text{C}_5\text{H}_5)_2$]

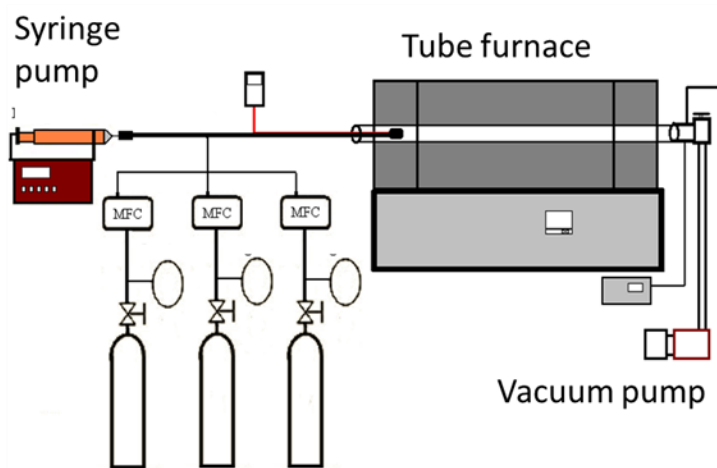


FIG. 7. Schematic of growth setup.

and xylene [$C_6H_4(CH_3)_2$] mixture is then loaded into an injection syringe. The syringe pump will inject the precursor into the tube furnace at a rate of 2 ml/hr. Argon and hydrogen are flown through the tube at 50 sccm to aid growth and purge byproducts through the tube. Once the precursor reaches the furnace it will dissociate, giving free iron atoms and hydrocarbons. The iron atoms will diffuse on and into the substrate and coalesce to form nanometer-sized catalyst particles. Ferrocene is a desired catalyst as Fe has a strong CNT adhesion, favors carbon diffusion, and produces stock hydrocarbons during pyrolysis²⁷. The substrate's in-diffusion rate will affect the CNT growth, and for certain substrates, a diffusion barrier is required to get the proper rate. Once the minimal-sized catalyst particle has formed, hydrocarbons will dissociate into free carbon upon impact. Volatile byproducts get expelled with the carrier gases while carbon atoms will diffuse onto the catalyst particle. Once enough carbons have diffused, they will precipitate out to form the energetically favored cylindrical formation of graphene due to its low surface energy²⁹. This process continues and the catalyst particle will essentially weave the carbon nanotubes. Kumar³¹ *et al.* have purported two main mechanisms of growth: base growth and tip growth. When the catalyst particle has good adhesion to the substrate characterized by an obtuse contact angle, graphite rings will be nucleated out of the Fe particle and grow upwards. Tip growth is characterized by an acute contact angle of the catalyst and, as the nanotube nucleates, it pushes downward and actually lifts the catalyst off of the substrate pushing it upward. SEM images of our samples indicate base growth is the primary mechanism during our growth. Sustained growth is needed to get decently tall CNT forests. Table I summarizes the growth factors affecting morphology.

Ferrocene concentration seems to be the dictating factor in continuous growth.

Higher concentrations will produce excessive hydrocarbons that can clog the catalyst particle, while low concentrations do not generate sufficient CNT density to ensure vertical growth¹³. In this study, molar ferrocene concentrations range from

0.2%-3.0%, depending on the specific substrate, and has a large influence on the density of the forest. Higher concentrations giving a denser forest will increase the presence of defects, as well. Precursor volume will tend to dictate the forest height and ranges from 0.5-2.0 ml in this study. Larger precursor volumes tend to grow taller forests in a linear fashion once the proper ferrocene concentration has been found. Forest heights in our samples ranged from 5-70 μm . The substrates used in this study include quartz, silicon with a 3 nm layer of aluminum (Al/Si), and silicon with a 66 nm layer of Niobium followed by a 3 nm layer of aluminum (Al/Nb). All samples were standardized to be $10 \times 10 \text{ mm}^2$ in size for optical data collection. SEM images were used to determine relative density, height, and defect level.

Data Acquisition

Reflectance and transmittance measurements were taken with a Pike[®] integrating sphere accessory installed in a Varian[®] 680 FTIR spectrometer. This yields a total

TABLE I. List of growth parameters affecting the morphology and defect level.

- | |
|---------------------------------|
| • Molar Ferrocene Concentration |
| • Precursor Volume |
| • Precursor Injection Rate |
| • Carrier Gas Composition |
| • Growth Temperature |
| • Substrate |
| • Furnace Flow Pattern |

diffuse, directional-hemispherical reflectance and transmittance measurement. This accessory provides an angle of incidence of 8° impinging the samples. Arcos³ *et al.* have shown reflectance increases with the incident angle; therefore, our data has given us the lower limit of reflectance^{3,4,8}. The integrating sphere's configuration consists of a 3" diameter diffuse gold sphere with a HgCdTe detector. Liquid nitrogen was used to cool the detector before data was taken. The temperature has an effect on the detector's sensitivity. To maintain consistency during data acquisition, the signal level of the raw interferogram of the machine was checked between runs. The interferogram has a representative peak that is dependent on the temperature of the detector. This peak has an inherent variation on the scale of seconds, yet the peak was checked at the beginning and end of the sample's data gathering, which takes around an hour total. To help keep the peak consistent, specific amounts of liquid nitrogen were added to the detector during the run. The sphere has an input port for the radiation source, a sample port, and a detector port. A reflecting mirror located in the center of the sphere directs the incoming radiation with a sample and a reference position. When the mirror is in the sample position, the incoming intensity is directed upward toward the sample port. When toggled to the reference position, it directs the light downward to a side of the integrating sphere. For reflectance measurements, the ratio of the sample position to the reference position data would give the reflectance value of the sample as a percentage of unhampered radiation. To achieve transmittance data, the sample is placed in front of the input port so all of the transmitted radiation gets collected by the detector. Certain parameters in the spectrometer can be adjusted to change the incoming beam's width and intensity along

with speed of data collection. The sample port has an 18-mm diameter round hole to locate a sample. Since our samples were standardized to a size of $10 \times 10 \text{ mm}^2$, diffuse aluminum mounting slides compatible with the sample port were used. Once the sample was mounted to its slide, the slide had to be centered on the sample port. Care was taken to find the beam's center at the sample port, and a centering fixture was made to position the mounting slide close to the beam center.

Reflectance

Reflectance data acquisition of a sample consists of collecting data with the mirror in the sample position followed closely by a data run with the mirror in the reference position. The ratio of the sample to the reference data yields a value for the directional hemispherical reflectance of the sample. Since the reflectance of these samples is so low, it was thought that even the smallest scattering from the mirror or other fixtures in the sphere could have an effect on our data. Data was taken with the sample port completely open to see if there was a noticeable background. Fig. 8 shows a

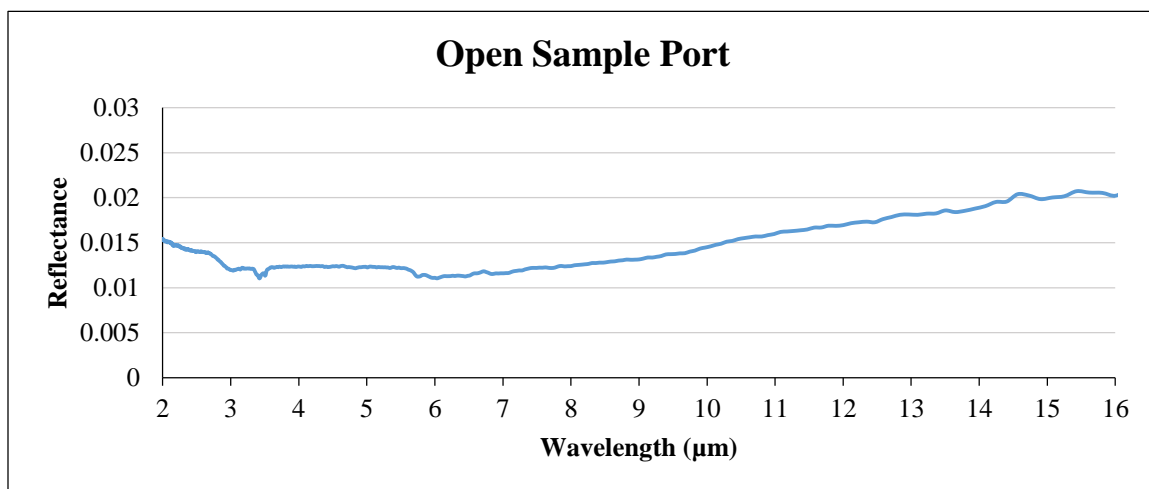


FIG. 8. Bare background signal of the integrating sphere.

typical result of such a run. Since the background is far from zero, a subtraction algorithm is in order to get a true reading of our sample's data. To accomplish this, an aluminum open slide with a diffuse surface was made with a $10 \times 10 \text{ mm}^2$ square hole machined out of the middle. Reflection data was taken of this open slide and was then subtracted from the samples data, so the reflectance can be written as

$$R = \frac{S_1}{R_1} - \frac{S_o}{R_o}, \quad (3.2.1)$$

where S and R designate the sample and reference mirror position, respectively, while the 1 and 0 subscripts represent the CNT sample and the open slide, respectively.

Justification of this algorithm is as follows. Let the incoming radiation from the source be I_o , which is reflected upward toward the sample from the mirror. The intensity coming off the mirror is equal to the incident intensity multiplied by the reflectance of the mirror. As depicted in Fig. 9, the light coming off of the mirror can be decomposed into two components, one denoted by ρ_{spec} (yellow), impinges onto the CNT sample and the other, denoted

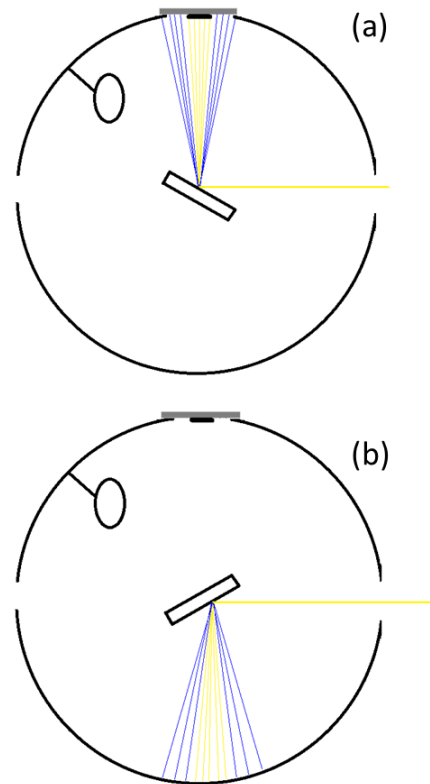


FIG. 9. Schematic of (a) sample, and (b) reference positions of the integrating sphere showing the two components of incoming radiation.

by ρ_{Diff} (blue), lands on the mounting slide and the side of the integrating. Therefore, the total intensity coming off of the reflecting mirror is

$$I_o(\rho_{Spec,M} + \rho_{Diff,M}). \quad (3.2.2)$$

Part of the incoming intensity will be reflected off of the CNT sample, and be designated

$$I_o\rho_{Spec,M}\rho_{Sample}, \quad (3.2.3)$$

while that coming off the mounting slide and integrating sphere wall will be

$$I_o\rho_{Diff,M}\rho_{Slide/Sphere}. \quad (3.2.4)$$

The addition of these last two expressions is then multiplied by the configuration factor, f_{Sample} , of the integrating sphere. This will be the intensity the detector collects, designated as S_1

$$S_1 = I_o(\rho_{Spec,M}\rho_{Sample} + \rho_{Diff,M}\rho_{Slide/Sphere})f_{Sample}. \quad (3.2.5)$$

The analytical representation for the reference position of the mirror is simpler than the sample position's. The reflectance from the mirror is not separated into components, but is rather the total reflectance, $\rho_{Tot,M}$. This, multiplied by the sample configuration factor of the sphere, gives

$$R_1 = I_o\rho_{Tot,M}f_{Sample}. \quad (3.2.6)$$

Now, the ratio of the sample position of the mirror to that of the reference is given as

$$\frac{S_1}{R_1} = \frac{(\rho_{spec,M}\rho_{Sample} + \rho_{Diff,M}\rho_{Slide/Sphere})}{\rho_{Tot,M}}. \quad (3.2.7)$$

Ideally, we would not like significant mirror scatter producing the two components for the sample position. The reason could be a lengthening of the optical path for the source light due to the addition of the accessory within the machine, since the light is focused and not collimated. If all of the light impinged onto the sample, no component separation would be necessary and $\frac{S_1}{R_1}$ would give the true reflectance of the sample.

An expression for the reflectance of the open slide is now in order. With the mirror in the sample position, the intensity coming off of the mirror is still split into two components. Now, however, the specular component of the reflectance off of the mirror escapes through the hole in the slide and is not collected from the detector. Therefore, only the diffuse component coming from the reflecting mirror striking the slide will contribute to the intensity collected by the detector. This multiplied by the configuration factor will give

$$S_o = I_o(\rho_{Diff,M}\rho_{Slide/Sphere})f_{Open}. \quad (3.2.8)$$

Note, the integrating sphere now has a different configuration factor; the difference being the area where the sample had occupied is now an opening. With the mirror switched to the reference position, the intensity that reaches the detector is

$$R_o = I_o\rho_{Tot,M}f_{Open}, \quad (3.2.9)$$

and the ratio is

$$\frac{S_o}{R_o} = \frac{\rho_{Diff,M}\rho_{SlideOpen/Sphere}}{\rho_{Tot,M}}. \quad (3.2.10)$$

Notice even though $\frac{S_1}{R_1}$ and $\frac{S_o}{R_o}$ have different configuration factors for the integrating sphere, they canceled when the ratio was taken. The same can be said about the incident intensities. Now, looking at the final expression, $\frac{S_1}{R_1} - \frac{S_o}{R_o}$,

$$\begin{aligned} R = \frac{S_1}{R_1} - \frac{S_o}{R_o} &= \frac{\rho_{Spec,M}\rho_{Sample} + \rho_{Diff,M}\rho_{\frac{Slide}{Sphere}}}{\rho_{Tot,M}} - \frac{\rho_{Diff,M}\rho_{\frac{Slide}{Sphere}}}{\rho_{Tot,M}} \\ &= \frac{\rho_{Spec,M}\rho_{Sample}}{\rho_{Tot,M}}. \end{aligned} \quad (3.2.11)$$

The mounting slide and the open aperture slide are made out of the same aluminum treated with a diffuse surface, and we are assuming they have exactly the same reflectance to get the last expression. This expression contains the reflectance of the CNT sample that we are looking for and two unknown factors that need to be considered. If we assume $\rho_{Spec,M} \gg \rho_{Diff,M}$, then $\rho_{Spec,M} \approx \rho_{Tot,M}$ and our algorithm would give an excellent approximation for the reflectance of the sample.

To check the final algorithm, 2% and 10% reflectance standards were purchased from Avian Tech[®]. We have taken data using our proposed method and compared it with the data provided from this company. The results for the 2% standard are shown In Fig. 10. The standards were large enough they could rest directly on the sample port to cover the whole area of the port. Notice, the data in the mid-IR region provided by the vendor is

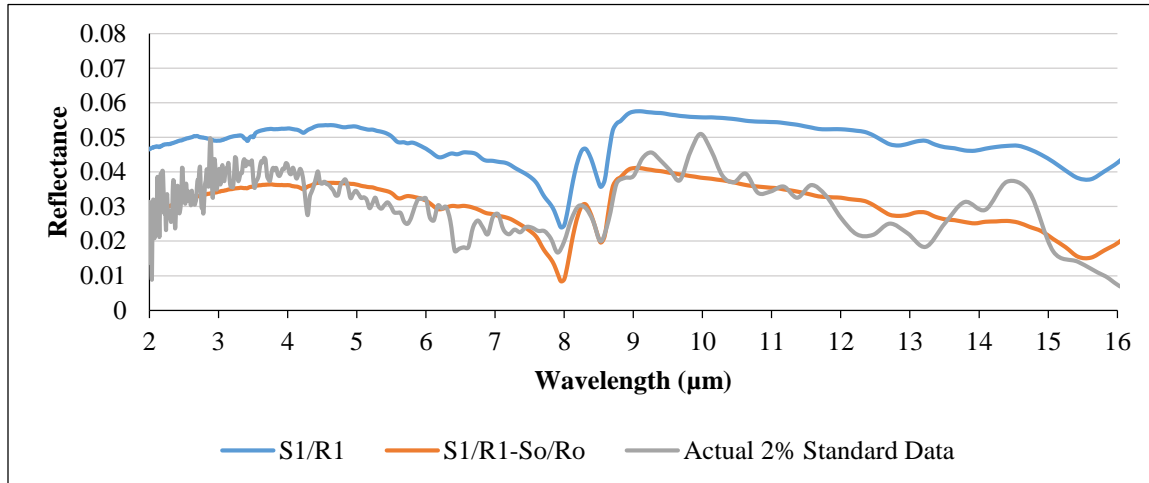


FIG. 10. Graph showing the reflectance data taken with and without the subtraction factor of the 2% standard compared with the data provided by Avian.

above the 2% reflectance specification in the near-IR region; however, it can be seen that our measurements agree reasonably well with the standard data.

Since the CNT samples were mounted on a square slide, data was taken in each of the four orientations and then averaged over these four runs. Early in the study, using the algorithm, negative values of reflectance were obtained for certain samples. To investigate this, operational settings of the machine were tweaked to see how it was affecting the final result. The parameter that has the primary effect was the aperture size that controlled the beam width as it entered the integrating sphere. There were five sizes of the aperture that were tested against the standards again to resolve this issue. The open mounting slide was set onto the sample port and the standard was then set onto the open mounting slide. This would mimic a $10 \times 10 \text{ mm}^2$ sample of the 2% standard. Once data was taken of the standard in this configuration, data was then taken for the subtraction portion of the algorithm. Data was taken repeatedly for all of the aperture settings and the results are shown in Fig. 11. It can be seen that data taken with a smaller aperture gets

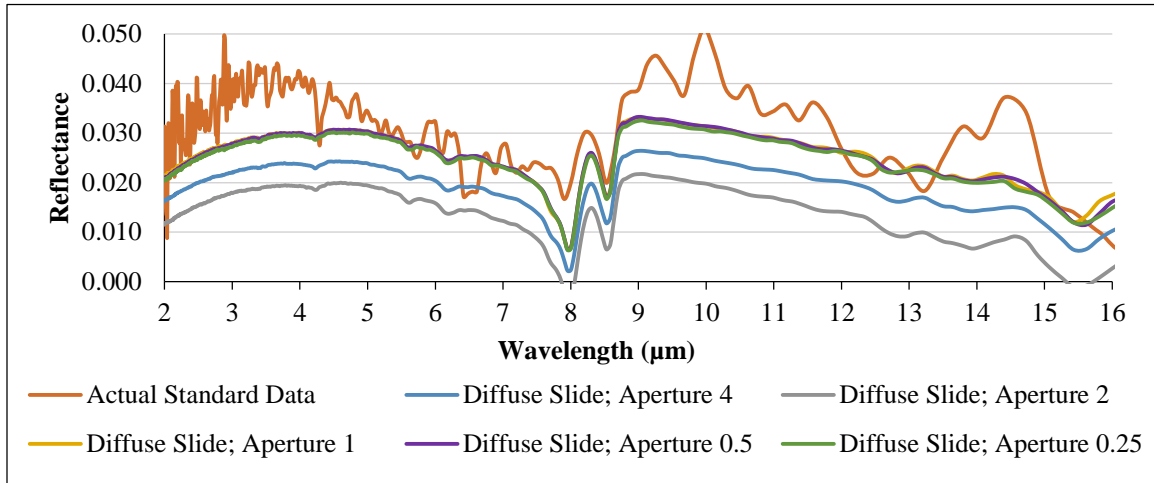


FIG. 11. Graph comparing the standard data to ours taken with various aperture sizes in the spectrometer.

closer to the standard's actual data. To further verify this effect, certain samples were selected and underwent the same investigation of the aperture size on the reflectance, as shown in Fig. 12 for Al/Si 127. It can be seen the smaller aperture size tends to raise the reflectance values up, the reason of which is not entirely clear at this point. Looking back at Eq. (3.2.11),

$$R = \frac{S_1}{R_1} - \frac{S_0}{R_0} = \frac{\rho_{Spec,M}\rho_{Sample} + \rho_{Diff,M}\rho_{\frac{Slide}{Sphere}}}{\rho_{Tot,M}} - \frac{\rho_{Diff,M}\rho_{\frac{Slide}{Sphere}}}{\rho_{Tot,M}} \quad (3.2.11)$$

$$= \frac{\rho_{Spec,M}\rho_{Sample}}{\rho_{Tot,M}},$$

if the beam width is increasing, this is effectively increasing the diffuse reflectance of the mirror, $\rho_{Diff,M}$, resulting in shifting the total reflectance of the mirror more towards the diffusive portion. However, this increase is the same for both the sample data and the open slide data. The only possible difference is the factor $\rho_{\frac{Slide}{Sphere}}$, which we assumed were

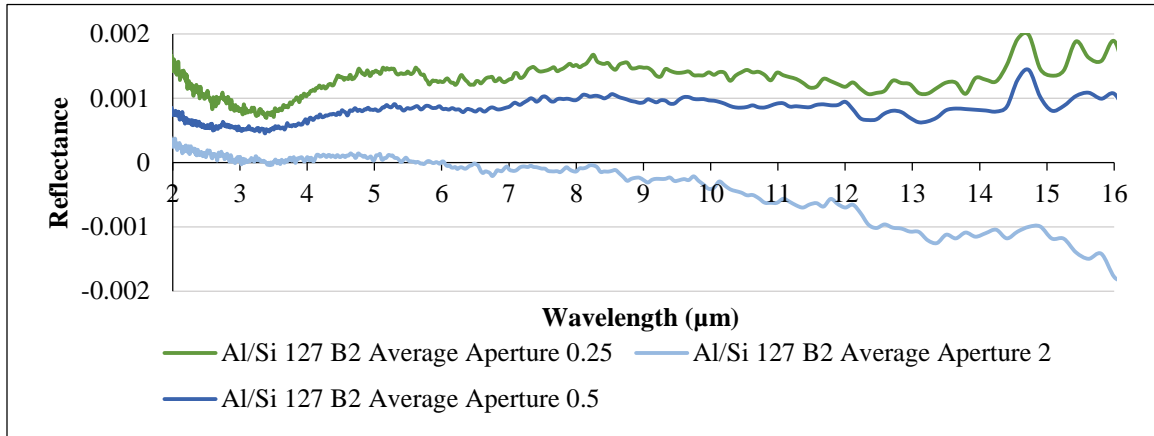


FIG. 12. Data taken on Al/Si 127 B2 with various aperture sizes of the spectrometer.

the same. If the sample has a high enough absorption, then ρ_{Sample} could be very close to zero. Then Eq. (3.2.11) is reduced to the difference between the reflectance of the open slide and the mounting slides. If the reflectance of the open slide, $\rho_{SlideOpen/Sphere}$, is greater, this could produce a negative value for the total reflectance. If the magnitude of $\rho_{Diff,M}$ is increasing, from a wide beam width, this will have an effect of exaggerating the reflectance discrepancy of the mounting slide to the open slide. Since the value for the total reflectance of the CNTs is very low, extreme care had to be taken to ensure the slides shared similar reflectance. This problem could be reduced in the future by using painted slides or slides of a dark absorbing material. Likewise, if the beam width is reducing, this is shifting the total reflectance of the mirror more toward the $\rho_{Spec,M}$ portion of the mirror's reflectance. From the data above, this is indicating $\rho_{Spec,M} \approx \rho_{Tot,M}$, and from our algorithm, this is implying

$$\frac{S_1}{R_1} - \frac{S_o}{R_o} = \frac{\rho_{Spec,M}\rho_{Sample}}{\rho_{Tot,M}} \approx \rho_{Sample}. \quad (3.2.12)$$

Transmittance

Transmittance data collection is simpler than that of the reflectance procedure. As mentioned before, to collect data the sample was mounted in front of the input port. This was accomplished with a machined plate that would secure the sample slide and center it close to the input port. A diffuse gold standard was placed over the sample port to help mimic a complete sphere. The reflecting mirror was positioned in the reference position for all runs. Now the sample configuration is that shown in the Fig. 13(a) with the sample fixed to the accessory and the mirror in the reference position, while that of the reference configuration is that of an open fixture in the input

port with the mirror still in the reference position. There is no need for a subtraction factor in the algorithm for the transmittance data. The ratio, therefore, is given as

$$T = \frac{S_1}{R_1} = \frac{I_o \tau_{sample} f_{trans}}{I_o f_{trans}} = \tau_{sample}. \quad (3.2.13)$$

The configuration factor cancels out again and we are left with the transmittance of the sample with this single factor, as desired.

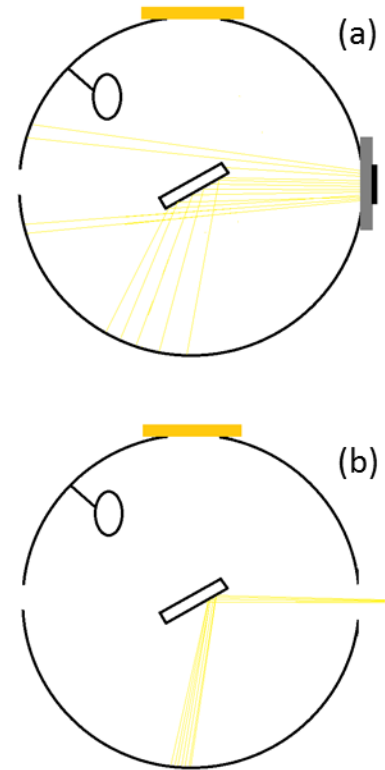


FIG. 13. Schematic showing the (a) sample, and (b) reference positions for transmittance data acquisition.

RESULTS

Once a reliable and absolute method of acquiring both diffuse reflectance and total transmittance of our samples has been established, correlation between the growth parameters to these values needs to be investigated. There are many growth parameters that will have an effect on the CNT forest morphology. The two primary factors are the precursor's ferrocene concentration and the precursor volume, which will affect the forest's density and height, respectively. Understanding the relation between the forest's morphology and the reflectance and transmittance values is done by varying one parameter, while keeping the other parameter constant. I have also studied these factors on various substrates. These results will cater the growth process for certain substrates to maximize the absorption of the CNT forest. The transmittance data of the samples will then be used to calculate the absorption coefficient and the skin depth of several CNT forests to investigate its reliance upon the morphology. It has been stated earlier the reflectance is split into two major

components, as seen in Fig. 14.

Incident intensity as I_0 strikes the surface of the forest. One reflective component comes from the top crust designated R_1 , along with a secondary reflection from the substrate designated as R_2 .

Depending on the absorption of

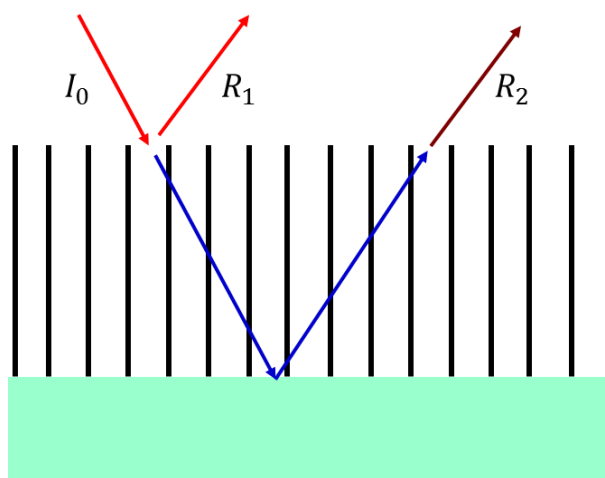


FIG. 14. Schematic of reflection components.

the forest, the substrate reflection may or may not reach the detector. The reflectance from the CNT film is heavily dependent on the condition of the top crust. Factors including the density, surface defects, and the level of entanglement affect the reflectance. Defects are related to the forest's density and include odd features on the surface consisting of bundles of CNTs grown on a catalyst caught on the surface or substrate chips that are pushed to the top from the substrate. CNT entanglement is formed at the beginning of the growth and is pushed to the surface by the subsequent growth. The amount of entanglement is related to the ferrocene concentration, as well. Therefore, we should expect the reflectance of the CNT film to depend only on the density of the forest, dictated by the ferrocene concentration of the precursor. The capability of the substrate reflection emerging from the forest depends on the reflectance and transmittance of the substrate and the absorption of the forest. Therefore, we expect the substrate contribution to depend on both the height and density of the film. Since transmittance is the sample's ability to let radiation enter and pass completely through the forest, we expect a dependence on both the density and the height of the forest. A denser forests should have a greater ability to absorb the radiation while it is traveling through the forest. The taller the forest, the longer the travel time through the sample, and hence, increases the chance for absorption.

Substrates

It is important to measure the reflectance and transmittance of the bare annealed substrates to understand the contribution they will have on the optical results. Three substrates were used in my study. The first was a silicon substrate with a 3-nm layer of

aluminum evaporated on its surface. The aluminum acts as a diffusion barrier for iron atoms once decomposed from ferrocene molecules. These substrates will be designated as Al/Si. The 2nd substrate is also a silicon base with a 66-nm layer of niobium followed by a 3-nm layer of aluminum, designated as Al/Nb. Finally, quartz was used as a substrate and requires no diffusion barrier for the iron catalyst. The higher the reflectance of these substrates, the stronger the substrate reflection collected from the sample's reflectance. The transmission of the substrate reveals how much radiation escapes the sample or how much gets absorbed into the substrate itself. Fig. 15 shows the reflectance of these substrates. The quartz substrate has relatively low reflectance over the spectrum, but has a strong reststrahlen³⁴ peak centered at 9 μm , giving a possible strong substrate reflection at this wavelength. Al/Si has a rather flat looking spectrum with a reflectance of about 40%. Al/Nb has a flat looking spectrum, as well, except for a dip near the shorter wavelengths. Its reflectance is rather high throughout with little transmission. Fig. 16 shows the transmittance of these substrates. It is clear the transmission of the Al/Nb

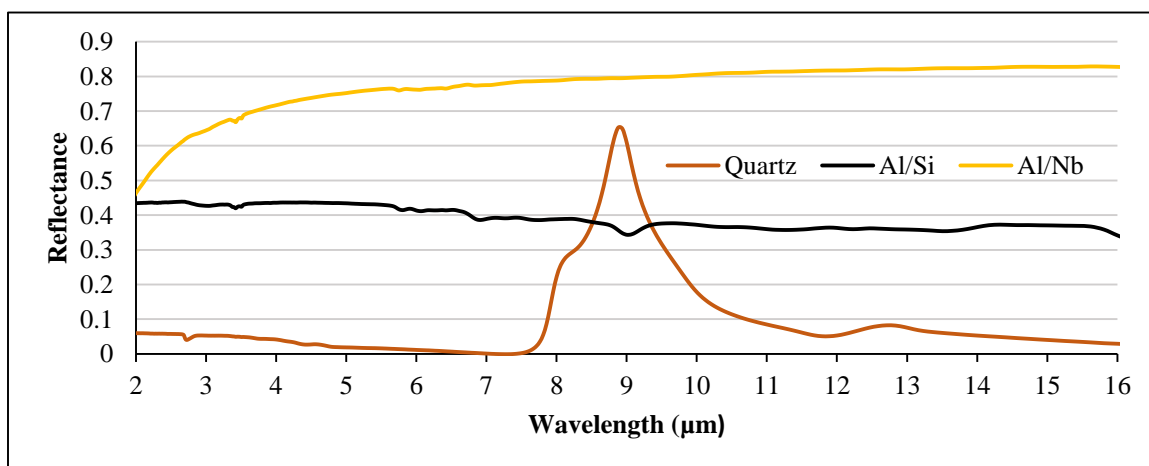


FIG. 15. Reflectance of the three substrates used for sample growth.

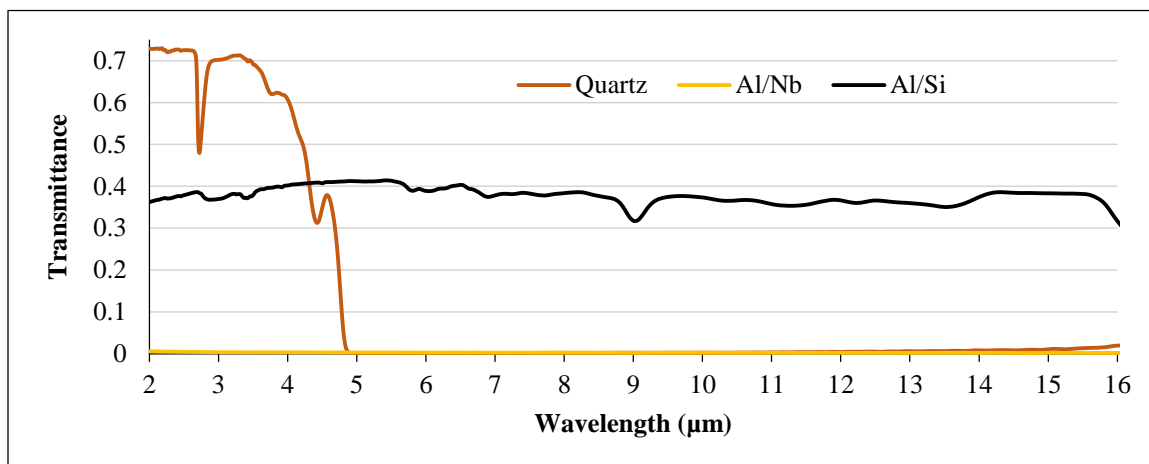


FIG. 16. Transmittance of the three substrates used for sample growth.

substrate is sufficiently low that the reflectance is the only concern. The quartz substrate has high transmission with some mild features in the range of 2-5 μm , followed by zero transmission beyond this range due to quartz's high absorbance and the strong reflectance at 9 μm . The transmittance of the Al/Si substrate is very similar to the reflectance values, where it is fairly flat throughout the entire spectrum.

Carbon Nanotube Forests

Aluminum/Silicon Samples

Table 2 shows the corresponding ferrocene concentration in the precursor and height measured from SEM imaging of five Al/Si samples. Al/Si 124 has the highest ferrocene concentration and hence, has the greatest density. Al/Si 127 and Al/Si 129 have a lower density than Al/Si 124, but

TABLE II. Ferrocene concentration and height of the five samples grown on Al/Si.

Sample	Height (μm)	Ferrocene (%)
Al/Si 124	12	1.5
Al/Si 127	24-27	0.5
Al/Si 129	42-51	0.5
Al/Si 132	24-28	0.2
Al/Si 133	42-49	0.2

are denser than Al/Si 132 and Al/Si 133. It can be seen that Al/Si 127 and Al/Si 129 have about the same density but Al/Si 129 is grown twice as long and hence, the height is about twice as high as Al/Si 127. Al/Si 132 and Al/Si 133 were grown to have similar density, but Al/Si 133 is roughly twice as tall as Al/Si 132. The SEM images of the top and side views of these samples are shown in Figs. A.1-A.3 in the Appendix.

Reflectance. Due to the lower density of samples Al/Si 132 and Al/Si 133, there is a significant substrate reflection, which creates interference fringes as depicted in Fig. 17. Since the radiation has to travel through twice as much forest in Al/Si 133 as that of Al/Si 132, most of the substrate reflection is absorbed by the forest. As a result, the fringes of Al/Si 133 is not as pronounced as those of Al/Si 132. This illustrates the amount of substrate reflection depends on the height of the forest. If the forest was even taller, it would have the capability to completely absorb the substrate's reflection. Growth of taller forests, however, has been difficult because of the limitation of the ferrocene to diffuse through the existing forest to the substrate. The density of Al/Si 127 and Al/Si 129 is

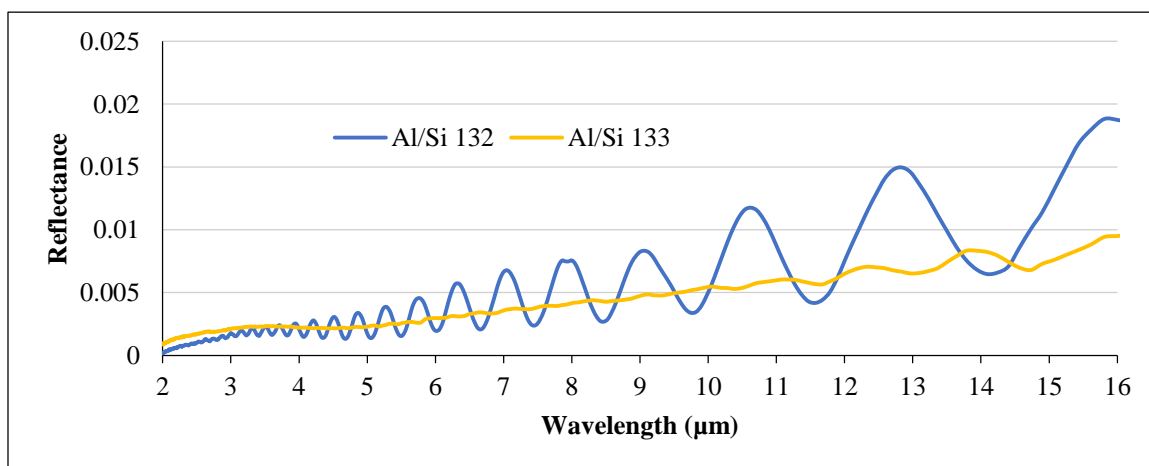


FIG. 17. Reflectance of lower density forests Al/Si 132 and Al/Si 133. Al/Si 133 is about twice as tall as sample Al/Si 132.

sufficient to absorb the reflection from the substrate and, hence, no interference is observed, as shown in Fig. 18. This leaves only the primary wave to contribute to the reflectance. It has been stated earlier that reflectance should depend mostly on the density of the forest and the amount of surface defects, and little on the forest's height. It can be seen the reflectance of Al/Si 127 and Al/Si 129 are very comparable to each other even though Al/Si 129 is about twice as tall as Al/Si 127. This suggests the CNT film reflectance has little dependence on the height of the forests. Comparing the reflectance of Al/Si 133 to Al/Si 129 shows the density effect on the reflectance since these two forests are of the same height. The denser forests of Al/Si 127 and Al/Si 129 seem to have a lower reflectance, however, it is misleading to conclude that denser forests lead to lower reflectance. The higher reflectance of Al/Si 133 is due to the contribution of the reflectance from the substrate. In fact, higher density should increase reflectance, as depicted in Fig. 18. Al/Si 124 has a large presence of surface entanglement, tube thickness, and defects that arise from an extreme concentration of ferrocene in the

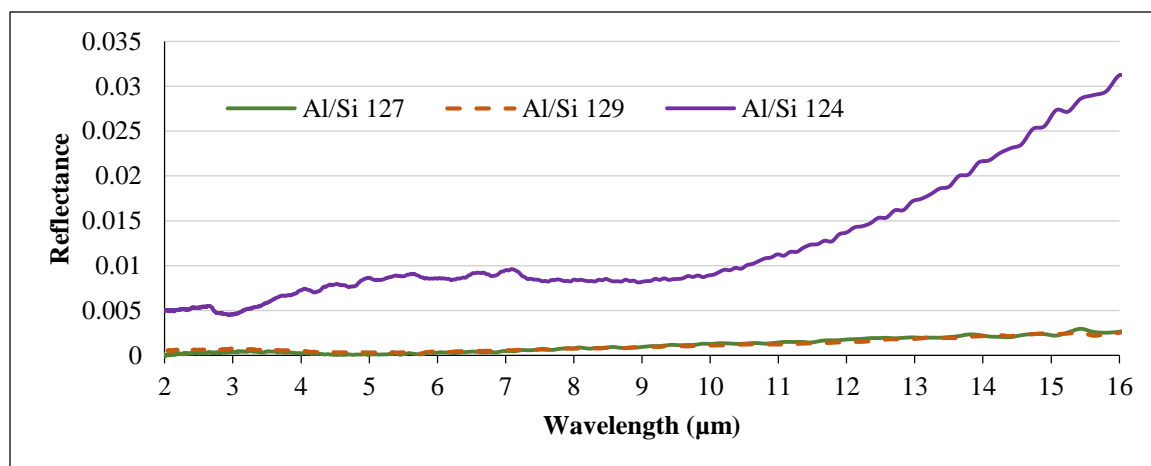


FIG 18. Reflectance of Al/Si 127, Al/Si 129, and Al/Si 124.

precursor, as shown in Fig. A.4. These features tend to enhance the overall reflectance of a sample.

In summary, the overall reflectance tends to be mainly dependent on the density of the forest. If the density is too high, the top crust will contain many surface defects, which increases the reflection of the radiation. If the density is too low, there will not be sufficient absorption to completely attenuate the substrate reflection, requiring a taller forest to make up for the discrepancy. Once the proper density has been found, the forest height will need to be catered to optimize the absorption of the whole sample. Ideally, all of the absorption would occur in the first pass down into the forest. If too much radiation makes it to the substrate, a portion of it will have the opportunity to be transmitted, which is not desirable for energy conversion applications.

Transmittance. The transmittance spectra for samples Al/Si 127, Al/Si 129, Al/Si 132, and Al/Si 133 are shown in Fig. 19. The transmittance of Al/Si 124 is close to zero due to the higher reflectance (toward the light source) and higher absorbance due to its

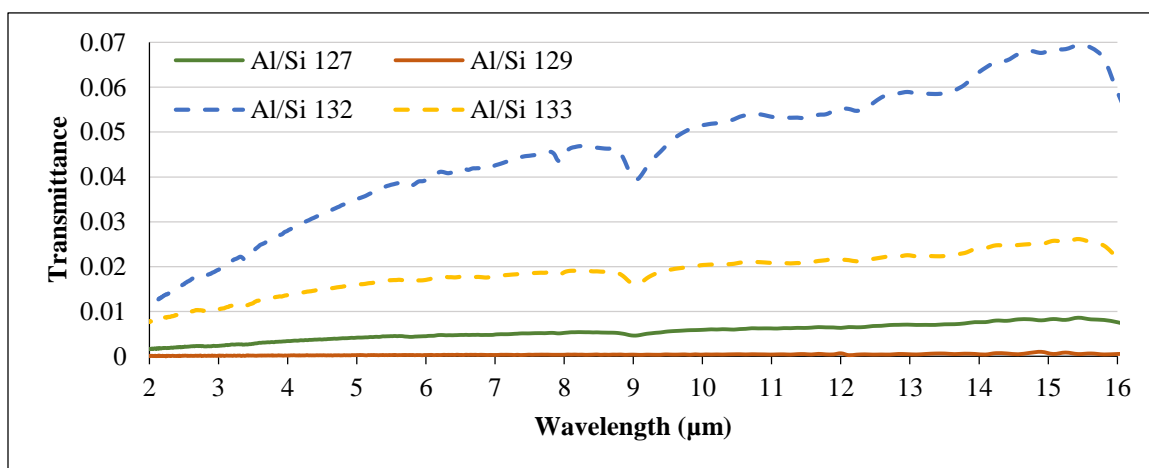


FIG. 19. Transmittance of all Al/Si samples except Al/Si 124 due to its near zero values.

ultra-high CNT density. Comparing the forests of the same density but varying heights will give us insight on the transmissions dependence on height. Fig. 19 shows the transmittance of Al/Si 127 is higher than Al/Si 129, consistent with the expectation since Al/Si 129 is twice as tall as Al/Si 127. Likewise, the taller forest of Al/Si 133 gives a lower transmittance than Al/Si 132. Therefore, with similar density the transmittance decreases with an increase in the forest's height. Given the fact Al/Si 127 and Al/Si 132 are about the same height, but Al/Si 127 has a higher ferrocene concentration than Al/Si 132 and hence, is denser, Al/Si 127 has a lower transmittance than Al/Si 132, reinforcing the notion that a greater density will decrease the transmittance. Similar results can be observed between Al/Si 129 and Al/Si 133.

To get the best absorption for a CNT forest, it appears we should first determine a proper density for the forest as this will let the radiation enter into the sample and help to attenuate the secondary reflected wave from the substrate. Once the density limit is known, then growing the tallest forest possible will absorb all the radiation by the time it reaches the substrate to eliminate any secondary reflection and transmission into the substrate.

Quartz Samples

Table 3 shows the growth parameters used for three samples grown on quartz substrates. Quartz acts as a good substrate for growth since it does not require a diffusion barrier for the iron catalyst. Results have shown a higher concentration of ferrocene is required to achieve forests of similar density to those grown on Al/Si. Quartz itself also has a very strong reflectance in the range between 7-10 μm and transmits very little light

beyond 5 μm , thus it gives a strong substrate reflection in these ranges.

SEM images comparing the denser sample of Q 125 to Q 130 is shown in Fig. A.4 in the Appendix.

TABLE III. Ferrocene concentration and height of three CNT forest samples grown on quartz.

Sample	Height (μm)	Ferrocene (%)
Q 125	11-16.5	3.0
Q 130	54-73	1.5
Q 134	14.5	1.5

Reflectance. Fig. 20 shows the reflectances of the samples grown on quartz. We obtained similar trends as from the Al/Si samples. Q 130 and Q 134 have similar densities but Q 130 is at least four times taller than Q 134. Q 134 has some slight interference fringes between 2-7 μm followed by a large reflectance in the 7-10 μm range due to the strong substrate reflection in this range indicating significant secondary reflection. Q 130 has a very low reflectance due to the absorption of the substrate reflection by the height of the forest. This is also an indication the density corresponding to a 1.5% ferrocene concentration gives a very small CNT reflectance from the top surface. Q 125 is as tall, but was grown with twice as much

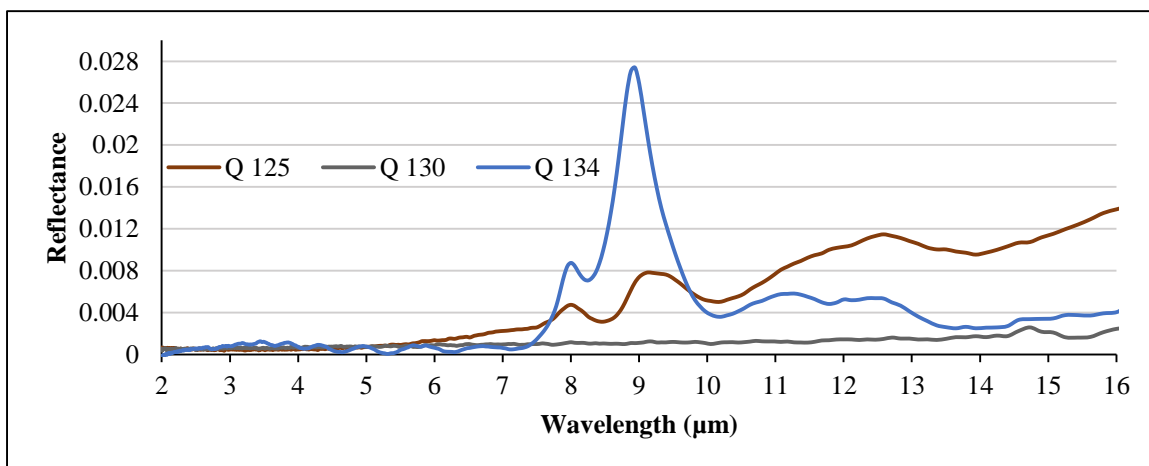


FIG. 20. Reflectance for samples Q 125, Q 130, and Q 134.

ferrocene as Q 134 and hence, shows a smaller peak in the 7-10 μm range. However, it has a higher reflectance in the longer wavelength range and shows a general increasing trend starting around 5 μm . An even taller forest may reduce this increase, however due to the already small CNT reflectance from the less dense Q 130, growth of taller dense forests was unnecessary and likely to produce defects. Similar to the Al/Si samples, once the proper density has been found to minimize the primary reflectance, the forest height is grown to completely absorb the secondary reflection from the substrate, ideally before the photons reach the substrate.

Transmittance. Transmittance of sample Q 130 was zero for the entire spectrum and thus is not included in Fig. 21. Note the graph stops at 5 μm since quartz transmits very little beyond this wavelength. Again, we see similar trends with the transmittance dependence on height and density as with the Al/Si samples. Q 134 and Q 130 have similar densities, but the shorter forest of Q 134 shows some transmittance compared to the zero transmittance of Q 130. Q 125 and Q 134 have similar heights, but Q 125 is

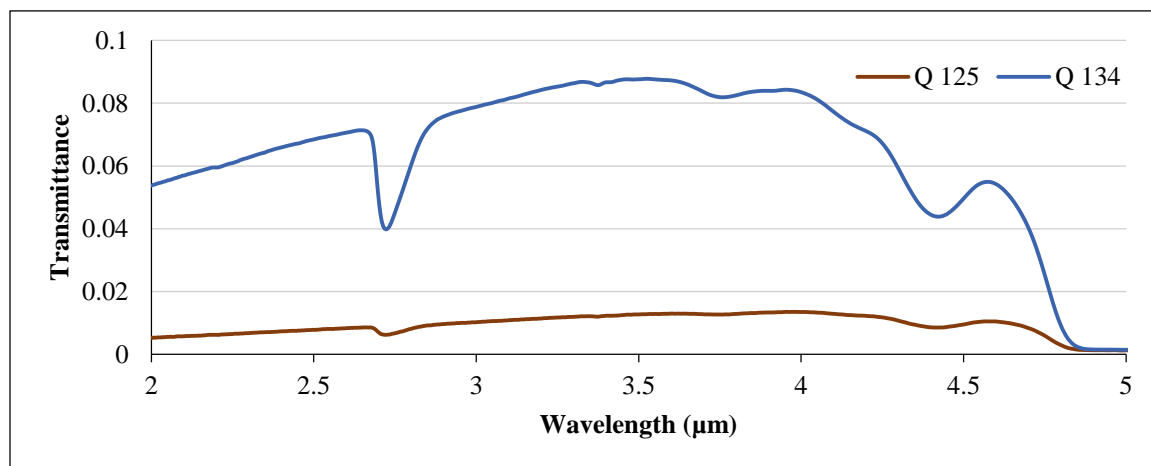


FIG. 21. Transmittance of samples Q 125 and Q 134.

denser and hence, shows a lower transmittance. It should be noted that quartz gives a nonzero transmittance beyond the 5 μm range. Fig. 22 shows the transmittance of all the samples centered around this region. As long as some light makes it to the substrate, the quartz will transmit about 0.15% percent of it. Q 130, however, had eliminated the radiation before it reached the substrate, and thus, transmits none. For the Al/Si samples, a ferrocene concentration of 0.5% was needed to get the proper density, but quartz required three times that to get the desired density. Despite these differences, forest morphology seems to dictate the optical properties for quartz substrates as they do for the Al/Si substrates.

Niobium/Aluminum/Silicon Samples

Table 4 shows four samples grown on silicon substrates with first a 66-nm layer of niobium, followed by a 3-nm layer of aluminum and will be designated as Al/Nb. Their ferrocene concentrations are similar to the Al/Si samples, but with smaller height differences that will still affect the results. These ferrocene concentrations give the

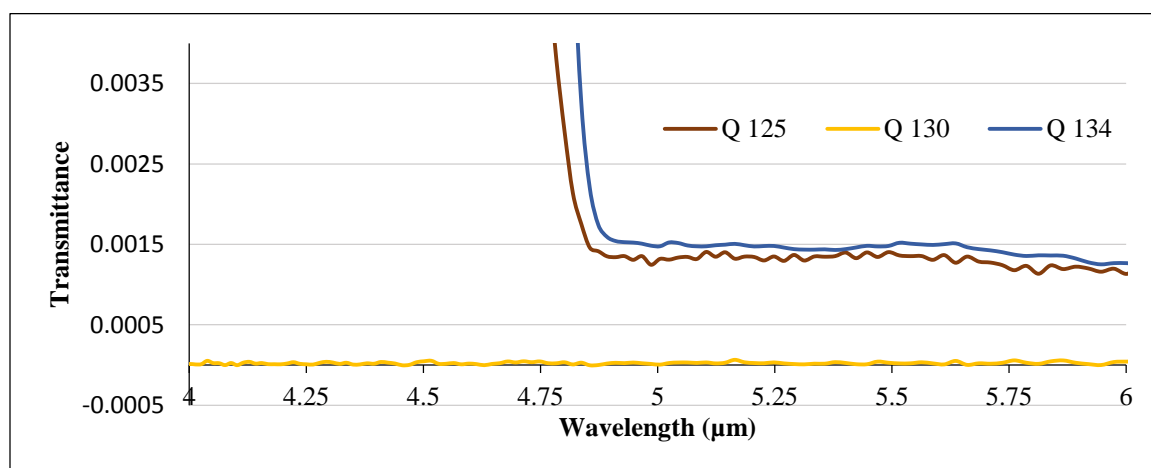


FIG. 22. Transmittance of all quartz samples focusing on the region of 5 μm .

desired density of the forests for absorption. The substrate is highly reflective with a relatively flat spectrum, therefore enhancing the reflection over the entire wavelength range. Al/Nb

TABLE IV. Ferrocene concentration and heights of four samples grown on Al/Nb.

Sample	Height (μm)	Ferrocene (%)
Al/Nb 126	16.5-18.4	0.5%
Al/Nb 128	22-24 μm	0.5 %
Al/Nb 131	18-20 μm	0.2 %
Al/Nb 135	20-22 μm	0.2 %

substrates produce a unique feature displayed in Fig. A.5 in the Appendix, showing a distinct surface corrugation. This is a result of the annealed substrate producing valley to peak differences around 300 nm. Energy dispersive X-ray analysis has shown Nb concentration is lower in the valleys, promoting growth in these regions and hence, produces random CNT surface modulations on the scale of microns. The low reflectance of these samples is believed to be attributed to these features and is corroborated by Ref. [31].

Reflectance. Fig. 23 shows the reflectance of two forests of the same density, but Al/Nb 128 is a little bit taller than Al/Nb 126. Note, both of these data show a lot of noise due to the very low input signal the detector collected. However, it is still noticeable the taller sample, Al/Nb 128, has a lower reflectance than the shorter, Al/Nb 126, which shows some signs of interference, as well as evidence the substrate reflection is strong, even for these very low reflectance values. Similar results are seen in Fig. 24 showing the less dense samples, Al/Nb 131 and Al/Nb 135. Al/Nb 135 is taller than Al/Nb 131 and hence, has a lower reflectance and does not show any interference fringes. The data were not as noisy due to the higher input signal the detector received. The total reflectance of

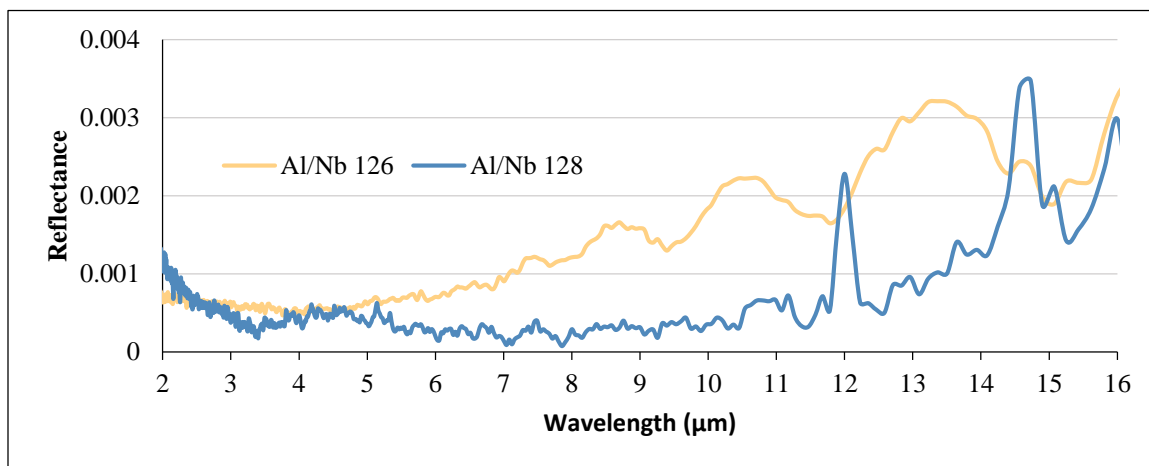


FIG. 23. Reflectance of the denser Al/Nb samples of 0.5% ferrocene concentration, but with different heights.

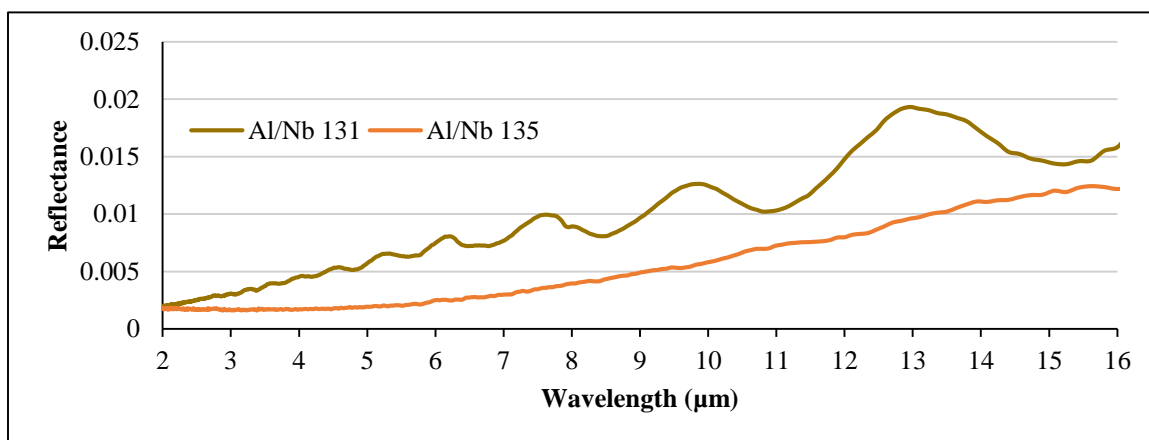


FIG. 24. Reflectance of the less dense Al/Nb samples of 0.2% ferrocene concentration, but with different heights.

these samples is higher than the denser samples shown in Fig. 23. Al/Nb 128 and Al/Nb 135 have similar heights, but Al/Nb 128 has lower reflectance due to its higher density, likewise for Al/Nb 131, and the denser Al/Nb 126.

Transmittance. Since Al/Nb substrate is highly reflective, and due to the thickness of the deposition layers, the transmittance of even the bare annealed substrate is very low.

Therefore, the transmittance of all the samples is very inconsistent and noisy, so it is not shown here. Suffice it to say the transmittance of all the Al/Nb samples is zero and all the incoming radiation is either absorbed or reflected by the sample.

It is a common trend that no matter what the substrate is, the density of the forest needs to be honed to reduce the level of defects and entanglement to provide the lowest CNT film reflectance. Varying ferrocene levels in the precursor is needed to accomplish this depending on the substrate used for growth. For the Al/Si and Al/Nb samples, 0.5% of ferrocene gives the best density in our study, while for the quartz samples, a concentration of 1.5% is needed. Once this concentration is known, a minimal height of the forest is needed to eliminate the refracted wave before it reaches the substrate. The minimal height can be revealed by the transmittance of the sample and also by the interference fringes in the total reflectance. Al/Si 129 at a height of 42-51 μm yields a practical zero transmittance and a reflectance no higher than 0.3%, making it the most absorbent of the Al/Si samples. Q 130 has a height of 54-73 μm and also gave a zero transmittance with a highest reflectance of 0.3%, as well. Al/Nb 128 has the lowest reflectance for this set of samples. With a height of only 22-24 μm , it has a near zero transmittance and a reflectance spectrum never reaches above 0.3% in the mid-IR range. We can, therefore, conclude conservatively these particular samples will absorb about 99.5% of light between 2 μm and 16 μm wavelength.

Absorption Coefficient and Skin Depth

The transmittance data were used with the Beer-Lambert law to extract the absorption coefficient. The coefficient is given as

$$\alpha = -\frac{1}{d} \ln \left(\frac{T_{sample}}{T_{substrate}} \right), \quad (4.3.1)$$

where d is the height of the forest found from SEM imaging, T_{sample} is the transmittance of the whole CNT sample and $T_{substrate}$ is the transmittance of a bare annealed substrate. The skin depth is defined as

$$\delta = \frac{1}{\alpha}. \quad (4.3.2)$$

The skin depth is the distance the radiation would need to travel to decrease its intensity by $1/e$, or roughly a third, giving us another way of determining a proper height of the forest to maximize absorption. This absorption coefficient will then be compared with two theoretical models to examine their ability to characterize a CNT forest.

Aluminum/Silicon Samples

The absorption coefficients of four of the Al/Si samples is shown in Fig. 25. Since Al/Si 124 has no transmission we cannot calculate its coefficient. Al/Si 129 is very noisy due to its height and very low transmittance, as well. The transmission of the Al/Si

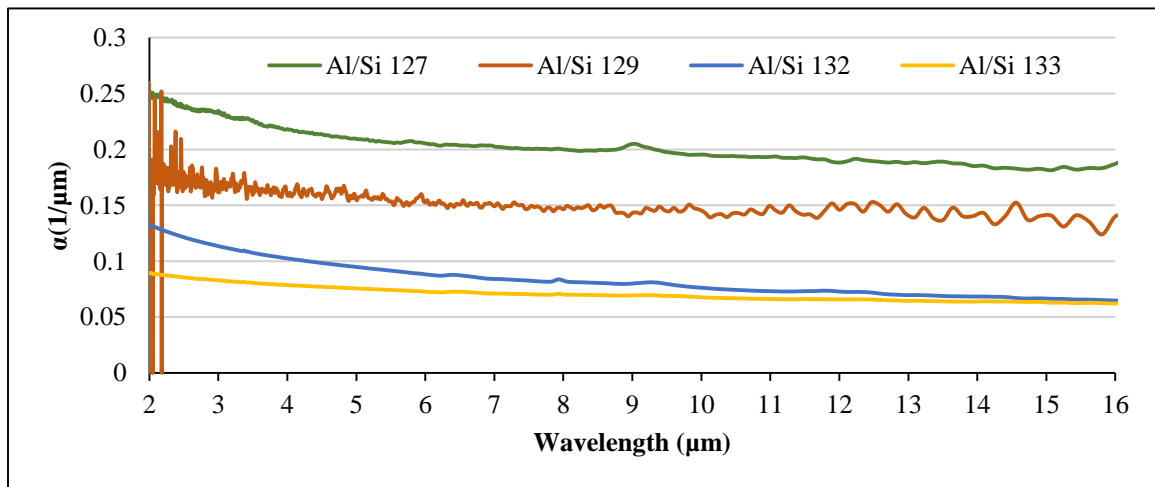


FIG. 25. Plot showing the absorption coefficient for the Al/Si samples.

samples is lower in the shorter wavelengths and hence, has a higher absorption coefficient in this region. A direct correlation between the density of the forest and the absorption coefficient can be seen by comparing Al/Si 127 to Al/Si 132, since they are of the same height, but different density. The denser forest of Al/Si 127 has a higher absorption coefficient than that of Al/Si 132. This can also be seen comparing the taller forests of Al/Si 129 and Al/Si 133. Consider the height's influence on the absorption coefficient by examining first Al/Si 127 versus Al/Si 129. It is clear the shorter forest of Al/Si 127 has a higher coefficient and hence, has a greater capability to absorb radiation. Since the coefficient is extracted from data where radiation passes completely through the forest, it is an averaged parameter encompassing the inhomogeneity of the forest. It has been shown with SEM imaging that the density of the forest decreases from tip to base¹³. This discrepancy is accentuated for taller forests, since a taller forest makes it harder for catalyst particles and stock carbon to reach the substrate and continue the growth. Therefore, a taller forest will have a greater portion of its height with lower density growth than that of shorter forests. Since the absorption coefficient is a reflection of this averaged density, it should have lower values for taller forests and be accentuated for shorter forests. This can be seen also with Al/Si 132 and Al/Si 133, as well, although their values tend to converge in the longer wavelengths. Comparison of the skin depths can be seen in Fig. 26. Small values for the skin depth means the radiation has to travel shorter distances to be attenuated. Equation (4.3.3) shows the transmittance,

$$T = e^{-\frac{d}{\delta}}, \quad (4.3.3)$$

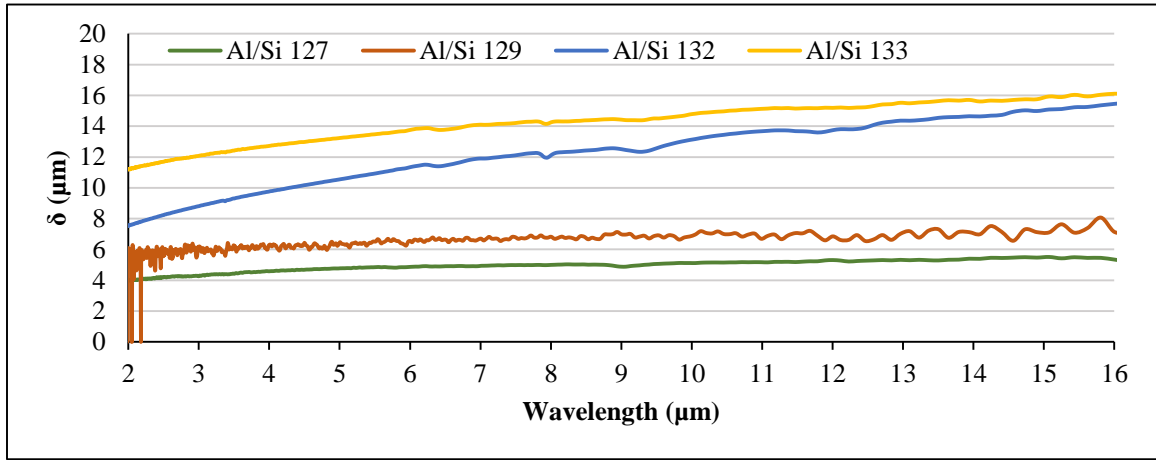


FIG. 26. Plot showing the skin depth for the Al/Si samples.

the radiation will experience in terms of the distance, d , it travels and the material's skin depth, δ . Table 5 shows values of T for various distances in terms of δ , showing the light would need to travel five times the skin depth to attenuate the radiation to about 0.7%. For example, the skin depth of Al/Si 127 is between 4-6 microns throughout its spectrum, so the light would need to travel between 20-30 microns to absorb all but 0.7% of the radiation. Al/Si 127 is 24-27 microns in height and its transmittance never gets above 1%, showing the skin depth is a good

indication of the height necessary to kill the transmitted light, making the sample an ideal absorber. It can be seen that this is a good approximation for other samples as well, and can even be used to narrow down the height ranges of the samples.

TABLE V. Table of T values for various distances, d .

d	T
$d = 1\delta$	0.369
$d = 2\delta$	0.135
$d = 3\delta$	0.050
$d = 4\delta$	0.018
$d = 5\delta$	0.007

Quartz Samples

Since quartz does not transmit past 4.75 microns, its absorption coefficient can not be calculated past this. Q 130 has no transmission at all and hence, we cannot calculate its coefficient. Fig. 27 shows the absorption coefficient for Q 125 and Q 134. They also show a trend of having a higher coefficient in the shorter wavelengths. The feature at 2.75 microns is attributed to the water absorption of the substrate when the ratio is taken³⁰. Q 125 and Q 134 are of the same height, but with Q 125 being denser. We see again the direct correlation between density and the absorption coefficient with these samples. Review of the height's influence on the coefficient could not be done since we were unable to calculate Q 130's coefficient. Fig. 28 shows the skin depths of these two samples, showing the denser Q 125 having a shorter skin depth. Again, theoretically, the forest height would need to be five times the skin depth to reduce the intensity to 0.7%. Since the skin depth of Q 125 is between 3-4 microns throughout its given spectrum, and its height being 11-16.5 microns, it could attenuate between 0.4%-6.4%, covering the range of values for its transmittance.

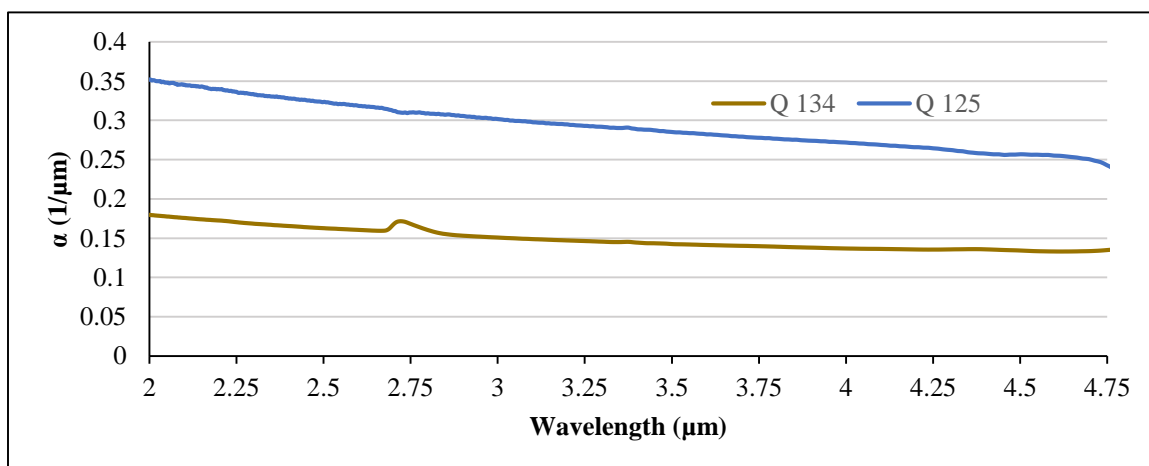


FIG. 27. Plot showing the absorption coefficient for the quartz samples.

Effective Medium Theory

Analysis of the EMT results is dictated by two fitting parameters, the alignment factor, X , and the filling factor, f . There are, in reality, infinite combinations of f and X that will produce the same curve, and thus physical reasoning is needed to help narrow down the choice of values. The filling factor is simply the area occupied by the CNTs and is directly proportional to the absorption coefficient. Considering hollow CNTs, the occupied area can be defined in terms of the inner and outer radii, r and R , respectively, and d , the distance between the tubes, which is shown by the relation

$$f = \frac{\pi(1 - \frac{r^2}{R^2})}{(2 + \frac{d}{R})^2}. \quad (4.4.1)$$

Using SEM images, we are allowed to determine average values for R and d . r cannot be measured directly and has to be estimated. Determination of these parameters was found only using images of the base of the forest, where typically the density is lower. Scraping is necessary to get a good cross section at the base for imaging, but also produce defects.

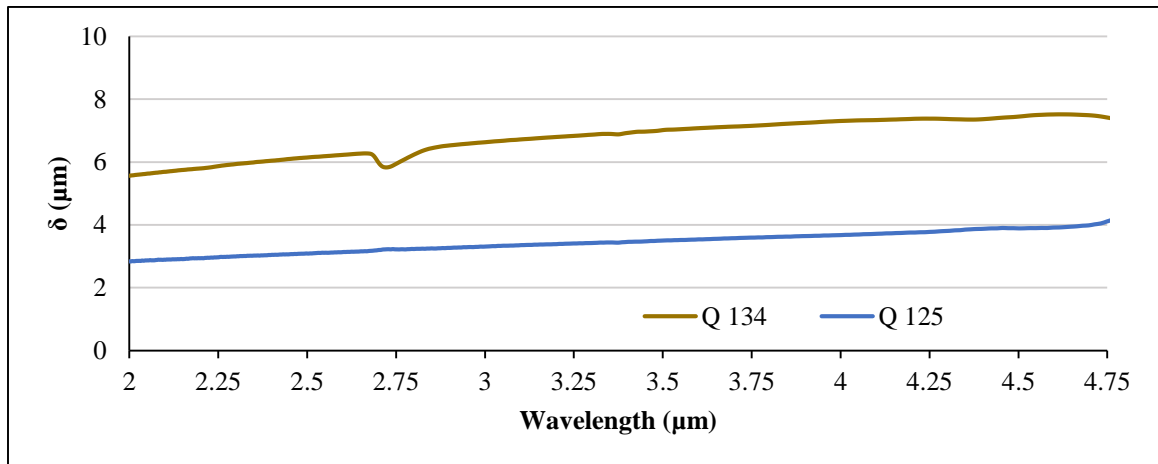


FIG. 28. Plot showing the skin depth of the quartz samples.

This, along with inhomogeneity throughout the forest, makes it difficult to get acceptable averages of these values. Similar values are observed for the Al/Si and quartz samples of 12 nm and 50 nm for R and d , respectively. Al/Nb samples showed similar outer radii, but with an average d value of 20 nm. This gives f values between 0.01-0.08 for the Al/Si and quartz samples and 0.08-0.23 for the Al/Nb samples. These numbers, however, are rather tentatively found and are used as a loose guide.

The alignment factor is a parameter describing the contribution of the effective dielectric of s-polarization. The spectrometer produces unpolarized light that is incident normal to the forest, giving random orientation of the electric field. Looking to Fig. 29 illustrates the contribution from each polarization component. Considering first an incident ray parallel to the tube's axis, the E field will impinge entirely perpendicular to the tube, corresponding to total contribution of ϵ_{eff}^p . With the tube lying flat, the E field of normal incident radiation may be directed either perpendicular or parallel to the tube axis, giving an equal contribution of ϵ_{eff}^p and ϵ_{eff}^s . Generalizing the above argument to a misaligned forest, the range of X

should be between 0 and 0.5.

Therefore, X can be a rough estimate of the alignment within the forest.

For this model, the absorption coefficient increases with both f and X , which means that ϵ_{eff}^s is the prime contributor to the

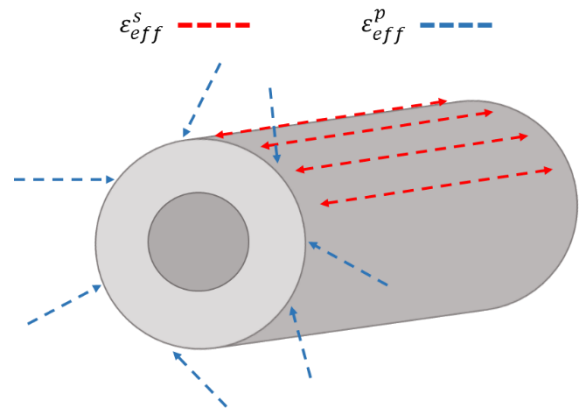


FIG. 29. Figure of electric field orientations and their designated polarizations.

absorption. It was found that X is the main factor in narrowing down the parameter space. If using the estimated f values given above, much too low values of X were needed to get close to the experimental data. The following section shows the ranges of f and X for each sample that yields the best fitting to the experimental data.

Aluminum/Silicon Samples

The results of the Al/Si samples are shown in Figs. 30-33, showing two best fitting curves based on EMT and their respective parameter values in Table 6. It is shown the two theoretical curves can fit exactly to each other. In fact, infinite number of curves can fit if the ranges of f and X are not limited. Although X is believed to range between 0 and 0.5, the plots show values of 0.6 and 0.9, as this range gives values for f closer to estimates from SEM imaging. These results show lower values of f for the less dense Al/Si 132 and Al/Si 133 samples as expected. The higher X values pushes f closer to its predicted values, giving a greater contribution from ϵ_{eff}^p ; hence, giving reasoning that

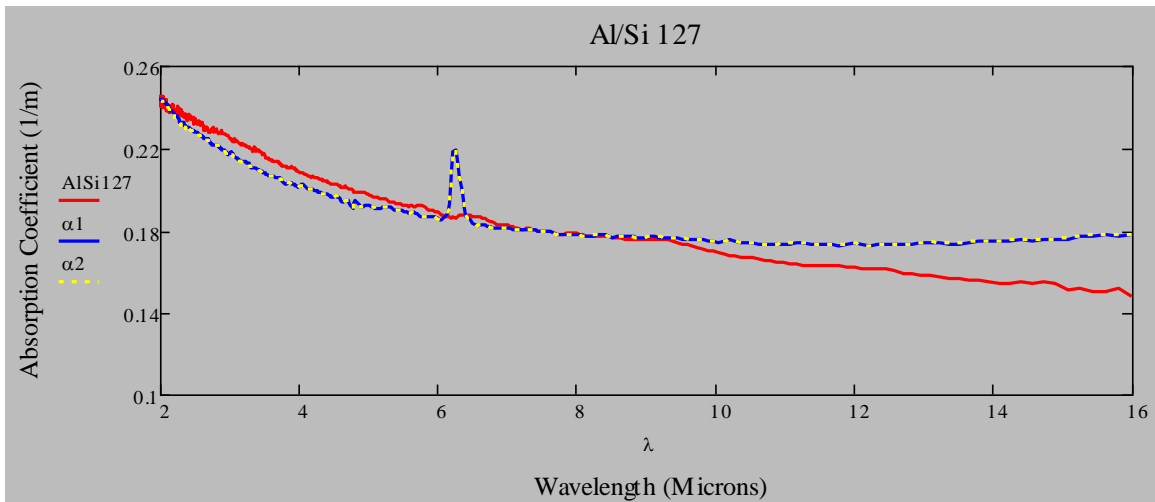


FIG. 30. Absorption coefficient of Al/Si 127 graphed with two EMT model curves.

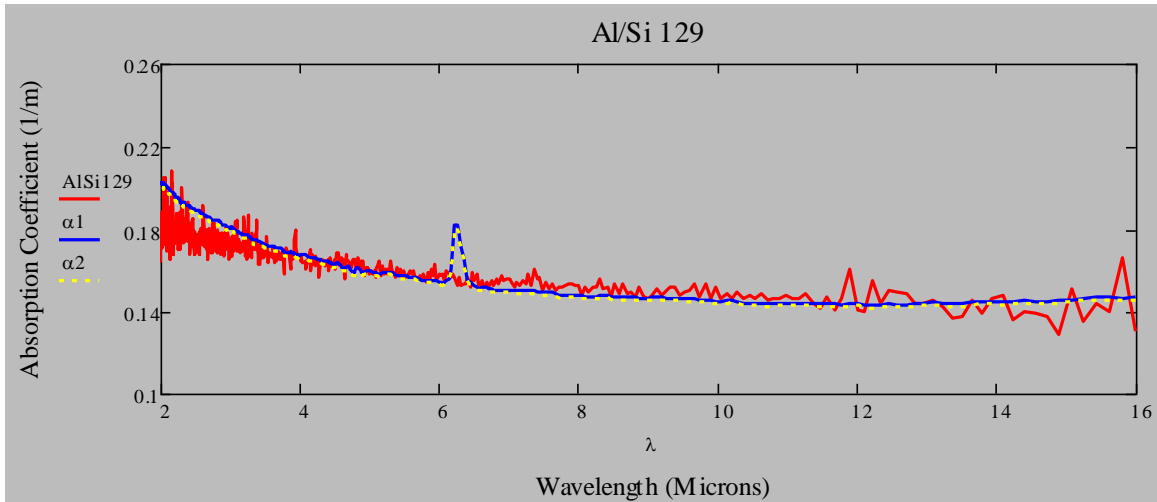


FIG. 31: Absorption coefficient of Al/Si 129 graphed with two EMT model curves.

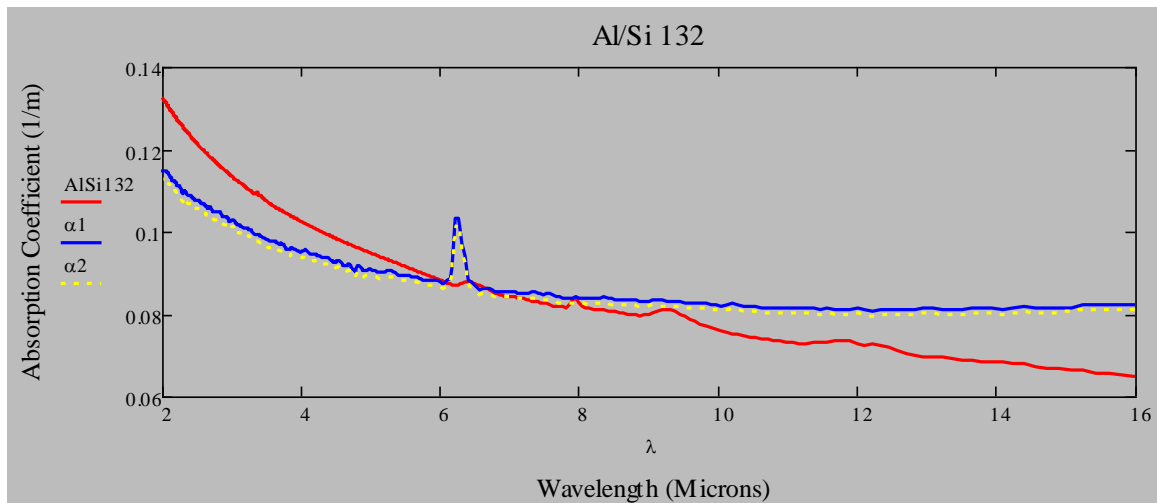


FIG. 32. Absorption coefficient of Al/Si 132 graphed with two EMT model curves.

there is a significant level of vertical alignment. The curvature of the theoretical model, especially at both ends of the spectral range, does not quite match the samples. The taller forests Al/Si 129 and Al/Si 133 seem to fit the model the best. This could be due to the fact that the taller forests have a greater portion of their composition with lower density growth than the shorter samples, and effective medium theory is intended to be used for

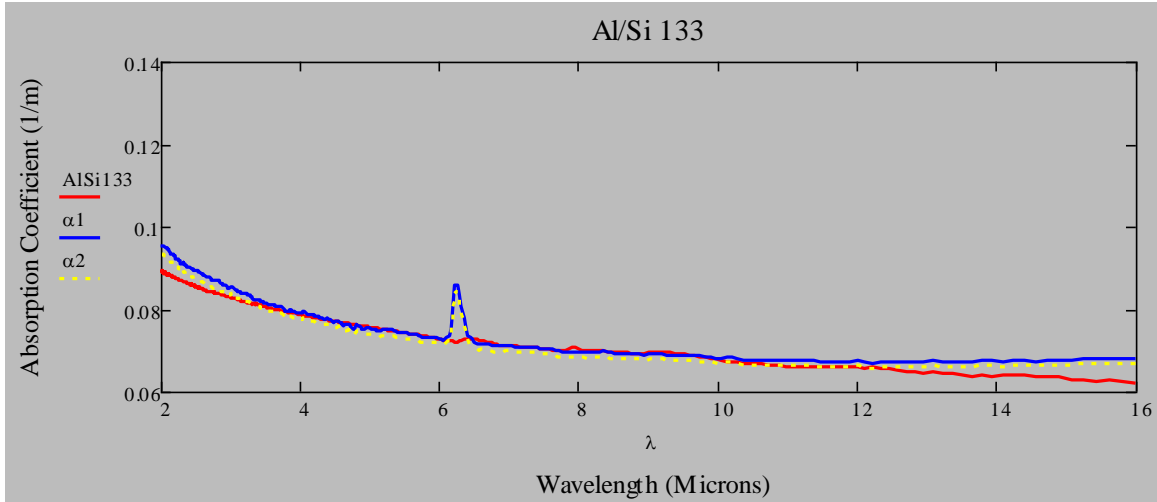


FIG. 33. Absorption coefficient of Al/Si 133 graphed with two EMT model curves.

TABLE VI. EMT parameters for Al/Si 127-Al/Si 133

Sample	Curve	f	X
Al/Si 127	$\alpha 1$	0.0095	0.6
	$\alpha 2$	0.038	0.9
Al/Si 129	$\alpha 1$	0.0075	0.6
	$\alpha 2$	0.03	0.9
Al/Si 132	$\alpha 1$	0.0043	0.6
	$\alpha 2$	0.017	0.9
Al/Si 133	$\alpha 1$	0.0035	0.6
	$\alpha 2$	0.014	0.9

sparse materials. Also, the absorption coefficient of the shorter forests of Al/Si 127 and Al/Si 132 show more uprising from changes in the shorter wavelengths. Extremely low or high values for X is the only way to alter the curvature of the theoretical curve, which is more prominent in the shorter wavelengths. Similar f and X values for samples of similar density are observed for the higher density samples, Al/Si 127 and Al/Si 129. Despite

their similar density, the difference between Al/Si 132 and Al/Si 133 in the shorter wavelengths is not clear at this point. The peak arising in the theoretical curves at 6.2 microns is a result of a discontinuity in ϵ_{\perp} from the raw graphite data.

Quartz Samples

Results for the quartz samples are given in Figs. 34 and 35 along with fitting parameters in Table 7. The absorption coefficient is limited to 4.8 microns, since quartz does not transmit beyond this wavelength. Here, the fits seem slightly better than the Al/Si samples, but this is mainly due to the fitting only being done in the shorter wavelengths. These results also show higher f values for the denser Q 125 sample. The shape of the experimental data for both samples are similar, but with the denser Q 125 having a larger range of absorption. Here, we also see a higher X value raises the f value closer to expectation. The peak in the Q 134 data were from the water absorption band and shows since this sample is less dense than Q 125.

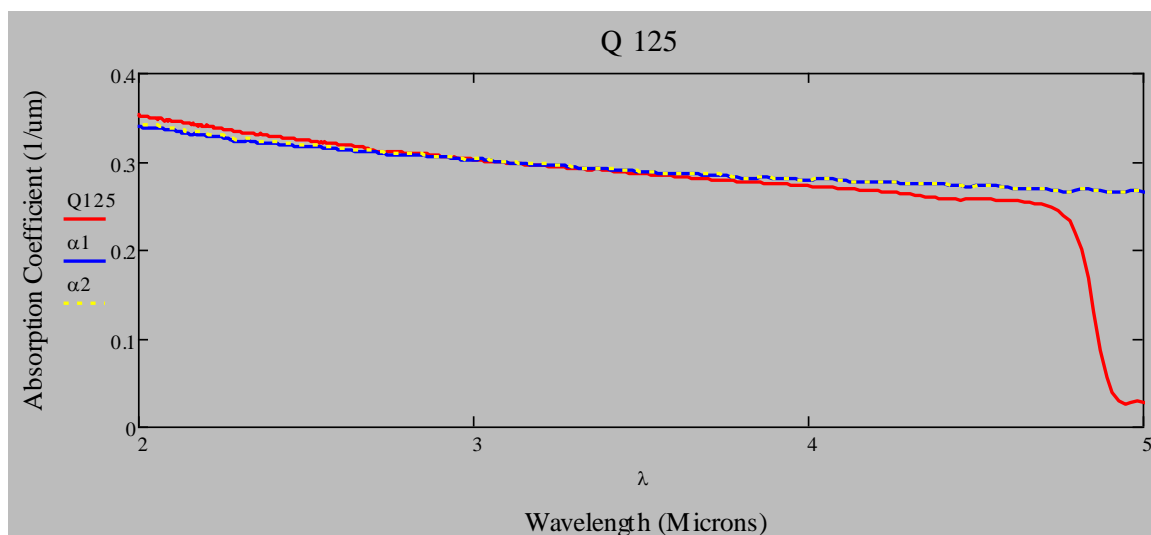


FIG. 34. Absorption coefficient of Q 125 graphed with two EMT model curves.

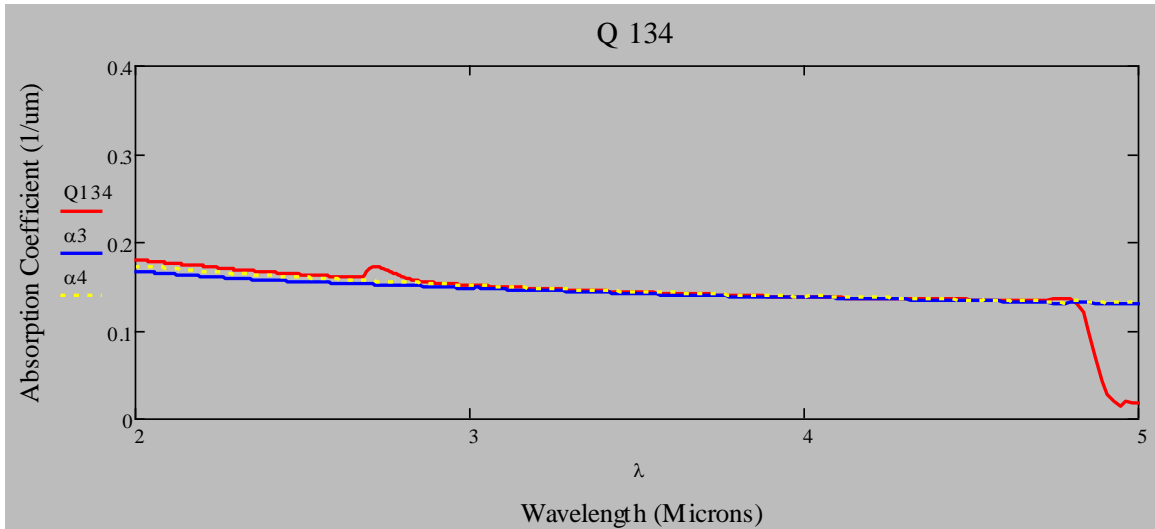


FIG. 35. Absorption coefficient of Q 134 graphed with two EMT model curves.

TABLE VII. EMT parameters for Q 125 and Q 134.

Sample	Curve	f	X
Q 125	$\alpha 1$	0.013	0.6
	$\alpha 2$	0.051	0.9
Q 134	$\alpha 1$	0.0063	0.6
	$\alpha 2$	0.025	0.9

Waveguide Model

The waveguide model produces three fitting parameters: the alignment factor, X , an effective radius of the waveguide, a , and a graphite conductivity reduction factor, S_0 . The definition of X is similar to that of the EMT model, but instead, it weighs the contribution of the perpendicular component of raw graphite, opposed to the contribution of the s-polarization dielectric function of the EMT model. Therefore, the range of its values cannot be argued the same as those for the EMT model. The waveguide model considers a collection of actual waveguides composed of graphite, the transmission

modes of which only allow E fields either total perpendicular or parallel to the wall. Since the waveguide is in actuality a CNT forest, the contribution from these components is averaged throughout the forest and X is thought to range between 0 and 1. Modeling is only carried out in the dominant TE_{11} mode that only allows E fields perpendicular to the walls of the waveguide. Therefore, a low X is expected for forests more vertically aligned. The effective radius is believed to be inversely proportional to the density of the forest, but a definite relationship is not yet achieved. S_0 is a factor reducing the conductivity, which signifies the difference between a CNT forest and bulk graphite. Since reducing conductivity increases radiation absorbed, S_0 can be related to the morphology of the forest. Since X also is a parameter related to the morphology, a loose correlation between X and S_0 is reasonable. Future experiments could lead to actual determination of S_0 , yet here we will use physical arguments to limit the range of S_0 . Again, there are infinite combinations of parameters to fit the data; therefore, we will use arguments to reduce the parameter space to find the lowest-order correlation. Increasing both the effective radius and X lowers the absorption coefficient and tends to affect the curvature of the theoretical curves. Once the minimum of these parameters is found that gives the best fitting, the smallest S_0 is used to match the data. Alignment with the quartz samples was not as successful shown in Figs. 40 and 41. The model shows similar patterns with the Al/Si and quartz samples, as we expect to obtain a smaller radius for the denser of them. Both quartz data required roughly the same larger X values and thusly, similar S_0 . However, they show similar S_0 with the taller Al/Si samples that have much lower X values.

Aluminum/Silicon Samples

Figs. 36-39 show samples of similar densities could be fit with the same effective radii and larger radii were needed for less dense samples, as expected. Their given parameters are summarized in Table 8. The shorter forests, Al/Si 127 and Al/Si 132, show a much higher X value than the taller Al/Si 129 and Al/Si 133 samples. This is an indication that there is a significant difference in the morphology between samples of

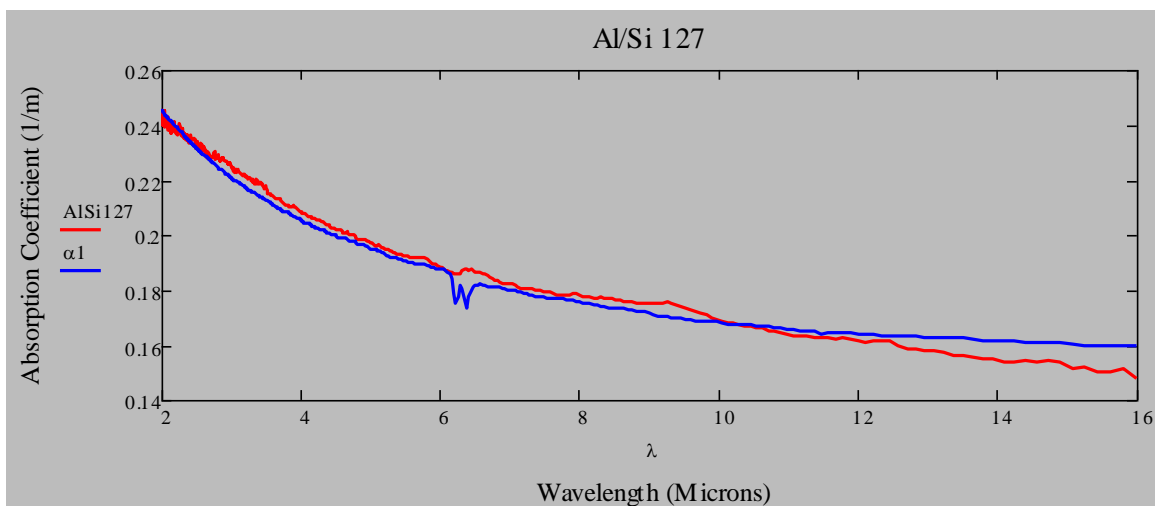


FIG. 36. Absorption coefficient of Al/Si 127 graphed with the waveguide model curve.

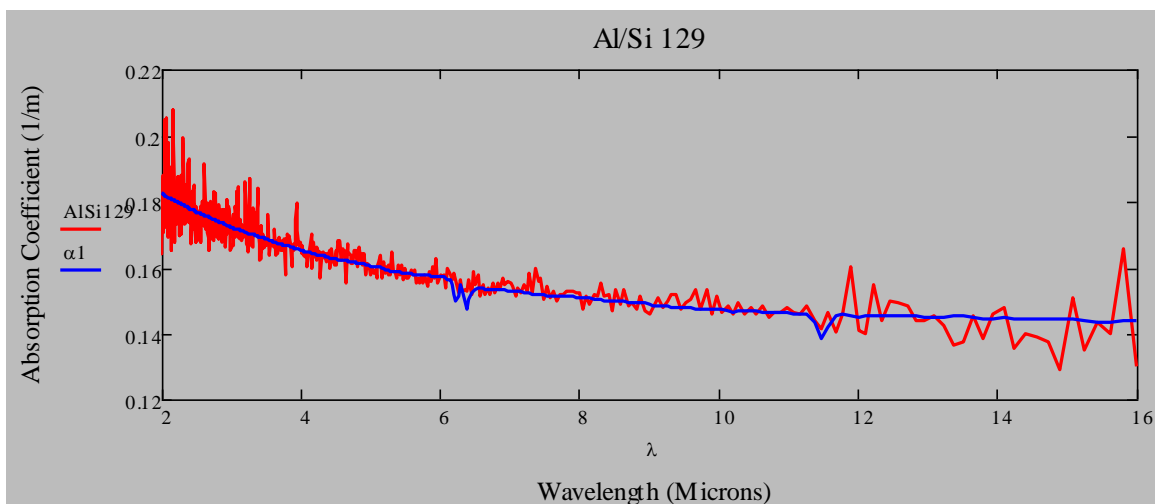


FIG. 37. Absorption coefficient of Al/Si 129 graphed with the waveguide model curve.

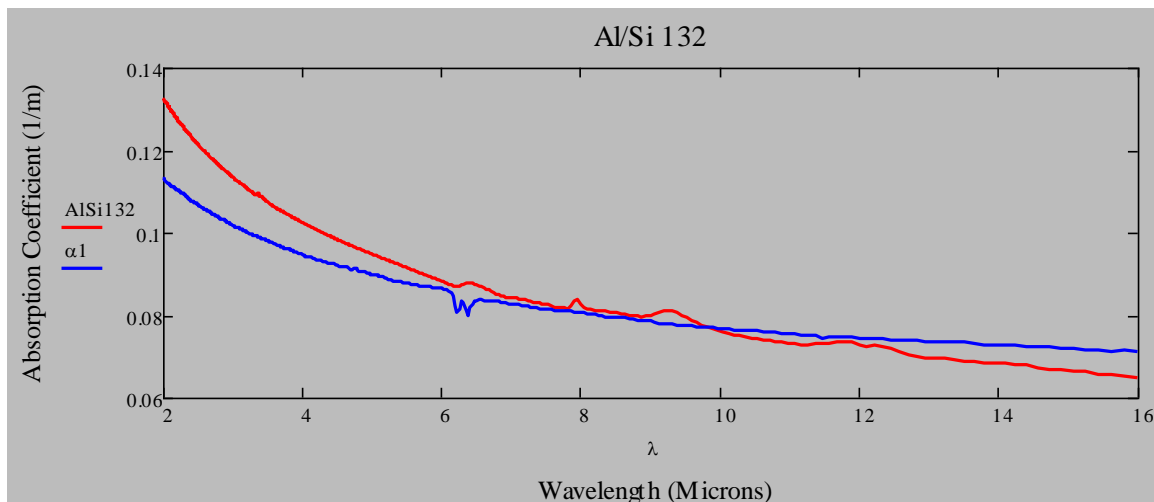


FIG. 38. Absorption coefficient of Al/Si 132 graphed with the waveguide model curve.

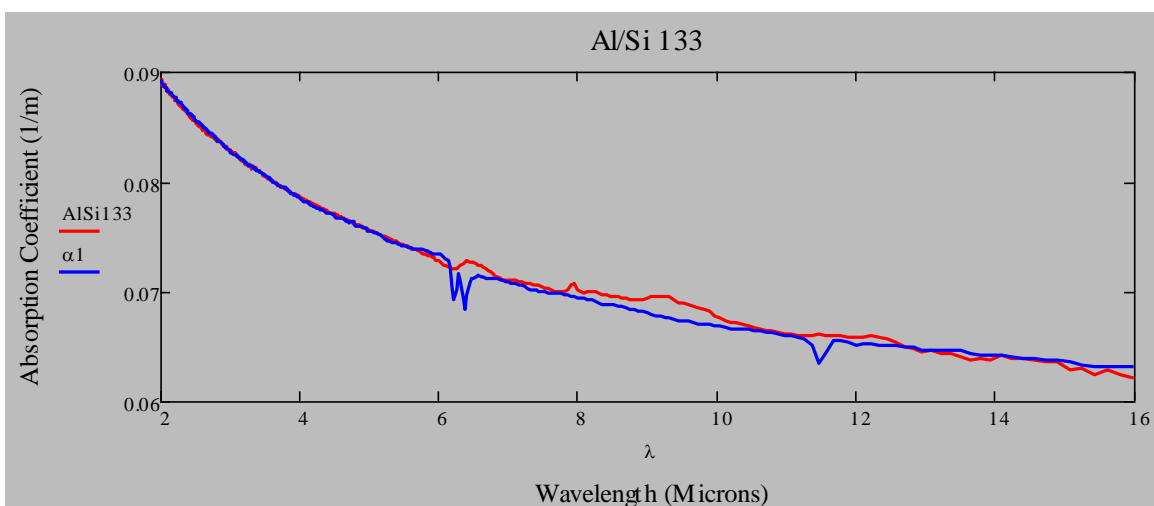


FIG. 39. Absorption coefficient of Al/Si 133 graphed with the waveguide model curve.

different heights, but grown with the same ferrocene concentration, giving the shorter forests a higher degree of misalignment. This is corroborated by looking at Fig. A.1 and Fig. A.2 in the Appendix. The factor X seems to be mainly dictated by forest height and is independent of the sample's density. It is also shown that X increases with S_0 . This indicates misalignment has a major influence on the conductivity, which physically

TABLE VIII. Waveguide parameters for Al/Si 127-Al/Si 133.

Sample	a (μm)	X	S_0
Al/Si 127	30	0.8	32
Al/Si 129	30	0.25	17
Al/Si 132	45	0.75	22
Al/Si 133	45	0.25	14

makes sense. The model tends to fit the shape of the experimental data better for the taller forests, which seems reasonable since these have a smaller fraction of misalignment.

Since we only consider the TE_{11} mode, only E fields perpendicular to the waveguide wall ($X = 0$) can propagate. Our results suggest longer tubes with smaller X values can be better approximated to an actual cylindrical waveguide. Similar to the EMT model, it also has trouble fitting the Al/Si 132 data, which has an accentuated curve to it.

Quartz Samples

Fitting with the quartz samples was not as successful as shown in Fig. 40 and Fig. 41 with their respective parameters shown in Table 9. This is due to the steeper decrease in absorption, especially in Q 125. This could be because of the smaller range of the data. Previous examples demonstrate theoretical curves often deviate more in the shorter wavelengths. Strong substrate reflection could affect the model's effectiveness to fit the data, as well. Since both quartz samples are roughly of the same height, they required roughly the same larger X values, as this seems to be independent of density, and thusly they share similar S_0 . However, they show similar S_0 with the Al/Si samples that have much lower X values, giving a conflicting relation between substrate species.

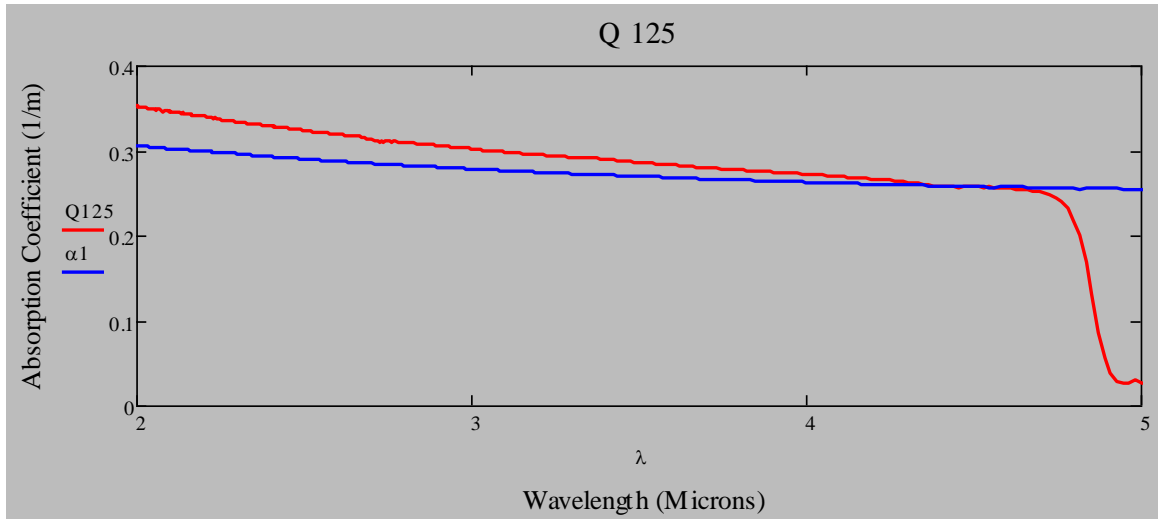


FIG. 40. Absorption coefficient of Q 125 graphed with the waveguide model curve.

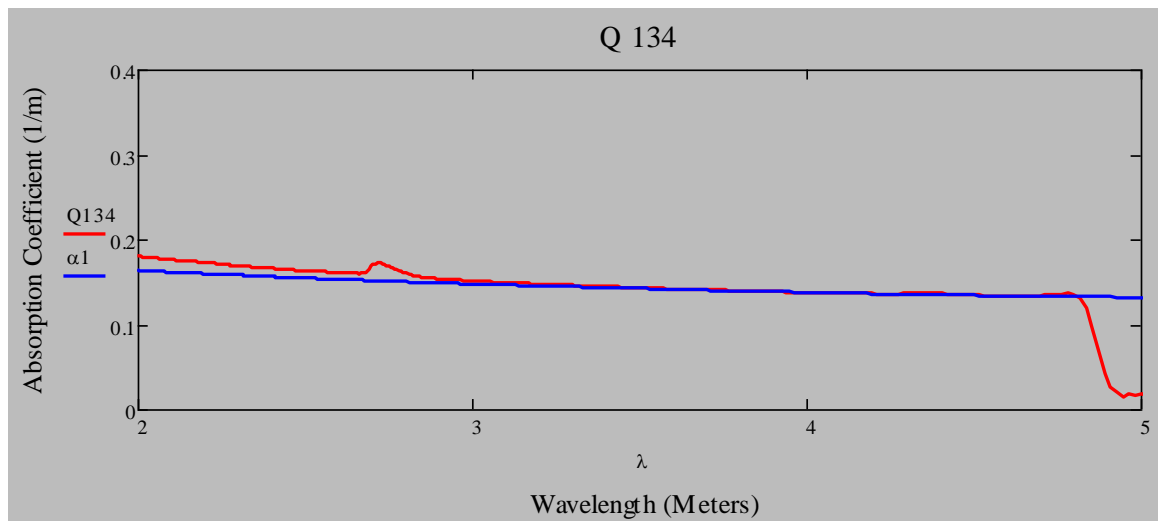


FIG. 41. Absorption coefficient of Q 134 graphed with the waveguide model curve.

TABLE IX. Waveguide parameters for Q 125 and Q 134

Sample	a (μm)	X	S_0
Q 125	10	0.8	13
Q 134	15	0.9	11

CONCLUSIONS

It was shown that at certain CNT density, a forest would reduce the reflectance of a sample, since the morphology of the CNT forest enhances absorption. The CNT absorption will reduce the reflection from the substrate, but higher CNT density will start increasing the CNT reflection. Having too high of a density will be detrimental to the reflectance as high concentration of ferrocene in the growth chamber creates secondary growth on top of the existing forest and surface defects. Once the proper density limit has been found for a particular substrate, the height of a sample can be tuned to eliminate the substrate reflection and the transmittance. From the transmission data, the absorption coefficient was found. Results show denser forests give a higher coefficient as expected. It also shows shorter forests have greater absorption than taller forests at a similar density due to a higher fraction of misalignment. For forests with the proper density, the skin depth of the Al/Si samples is around $7 \mu\text{m}$ while for the quartz samples it was about $4 \mu\text{m}$. These results suggest the Al/Si and quartz forests will need to be about 35 and 20 microns tall, respectively, to be completely absorptive. This height is well within our capabilities to produce with minimal defects. Although we were not able to calculate the absorption coefficient for the Al/Nb samples, the zero substrate transmission allows the absorption to be directly related to the reflectance, inferring the Al/Nb 126 and Al/Nb 128 samples are almost completely absorptive.

Effective medium theory uses a filling factor and an alignment factor to generate the absorption coefficient of a CNT forest. The filling factors were consistent with the density expectations, giving higher values for the denser forests. Samples of the same

density, but of greater height, have smaller filling values for f than their shorter counterparts. This is consistent with the experimental results, as the taller forests produce smaller absorption coefficients than the shorter ones, which is believed to be caused by inconsistent density in taller forests. For this model, the greater values for X gave f values closer to expectations based on SEM imaging. For the Al/Si samples, the spectra it produced did not quite fit the experimental data. The theoretical curves tend to have higher curvatures at both ends, producing more of a bowl shaped curve compared to the data. The fitting matches better to the taller Al/Si samples and it was able to fit the quartz data a little better than the waveguide model, but does not fit well for the shorter forest of Al/Si 132.

The waveguide model uses three fitting parameters; the effective radius of the waveguides, the alignment factor, and a reduction factor for graphite's conductivity. It has been shown the effective radius of the waveguide is inversely proportional to the CNT density, as predicted. Since analysis was done in the dominant TE_{11} mode, a true graphite waveguide should have $X = 0$. The difference of X between the tall and short Al/Si forests is consistent with the expectation. Additionally, X is independent of the effective radius and has higher values for the shorter forests, which is consistent with the observation that the shorter forests have a higher fraction of misalignment. The reduction factor appears dependent on the density and height of the forests. Samples of same height, but different density, show a higher reduction for the denser forests. Forests of similar density, but different height, however, show a more drastic change in conductivity, as the taller forests give less reduction. It seems the taller forests have

greater alignment and higher conductivity.

Overall, we have successfully connected the reflectance, transmittance, and absorption of carbon nanotube forests to their growth conditions and substrates, allowing us to create an almost completely absorbing sample. The success of applying the two models shown here seems to be rather contingent. The EMT model gives some physically sound results, but its curves fit less to the experimental data. The waveguide model also produces results that make sense, but its extra parameters need further experimentation to narrow down the values. Although it is hard to physically envision the CNT forest as a series of waveguides, the model has given us some more enlightenment. This study has given us a better understanding of the optical properties of carbon nanotube forests and broadens our knowledge for the future applications of these fantastic absorbers.

REFERENCES

- 1 H. Ye *et al.*, Appl. Phys. Lett. **101**, 141909 (2009).
- 2 E. Hecht, *Optics*, (Addison Wesley Publishing, San Francisco, 2002).
- 3 T. d. I. Arcos *et al.*, Nanotech. **18**, 265706 (2007).
- 4 H. Shi *et al.*, AIP, **99**, 211103 (2011).
- 5 Y. Murakami *et al.*, Chem. Phys. Lett. **385**, 298 (2004).
- 6 K. Mizuno *et al.*, Proc. Nat. Acad. Sci. **106** 6044-47 (2009).
- 7 M. A. Quijada *et al.*, Proc. SPIE **8150**, 815002-1 (2011).
- 8 X. J. Wang *et al.*, Nanotech. **20**, 215704 (2009).
- 9 J. G. Hagopian *et al.*, Proc. SPIE **7761**, 77610F-1 (2010).
- 10 K. F. Mak *et al.*, Solid State Comm. **152**, 1341 (2012).
- 11 C. H. Chang *et al.*, Optical Society of America, **36**, 12 (2011).
- 12 U. Platt and J. Stutz, *Differential Optical Absorption Spectroscopy: Principles and Applications*. (Springer-Verlag, Berlin, 2008).
- 13 R. W. Call, M.S. thesis, Utah State University, 2012.
- 14 F. J. Garcia-Vidal *et al.*, Phys. Rev. Lett. **78**, 4289 (1997).
- 15 F. J. Garcia-Vidal and J. M. Pitarke, Eur. Phys. J. B. **22**, 257-265 (2001).
- 16 B. T. Draine and H. M. Lee, Astrophys. **285**, 89-108, (1984).
- 17 J. B. Pendry and A. Mackinnon, Phys. Rev. Lett. **69**, 2772 (1992).
- 18 J. B. Pendry, J. Mod. Opt. **41**, 209 (1994).
- 19 A. J. Ward and J. B. Pendry, J. Mod. Opt. **43**, 773 (1996).
- 20 W. Lü and J. Dong, Phys. Rev. B. **63**, 033401 (2000).

- 21 C. F. Bohren and D. R. Huffman, *Absorption and Scattering of Light by Small Particles*, (John Wiley & Sons, Hoboken, New Jersey, 1998).
- 22 L. Henrard and Ph. Lambin, *J. Phys. B. Mol. Opt. Phys.* **29**, 5127-5141 (1996).
- 23 N. W. Ashcroft and E. R. Mermin, *Solid State Physics* (Saunders College, New York, 1976).
- 24 D. M. Pozar, *Microwave Engineering*, (John Wiley & Sons, Hoboken, New Jersey, 2012).
- 25 S. Iijima, *Nature (London)* **354**, 56 (1991).
- 26 M. Zhang *et al.*, *Chem. Phys. Lett.* **336**, 3-4, 196-200 (2001).
- 27 M. Kumar, *Carbon Nanotubes-Synthesis, Growth and Applications*, (In-Tech Publishers, Shanghai, 2011).
- 28 S. F. Ren *et al.*, *Science*, **282**, 1105 (1998).
- 29 G. G. Tibbetts, *Cryst. Growth* **66**, 632-838 (1984).
- 30 J. B. Heaney *et al.*, *Appl. Opt.* **22**, 244069 (1983).
- 31 Z.-P. Yang *et al.*, *Appl. Opt.* **50**, 1850 (2011).

APPENDIX: SEM Images of Samples

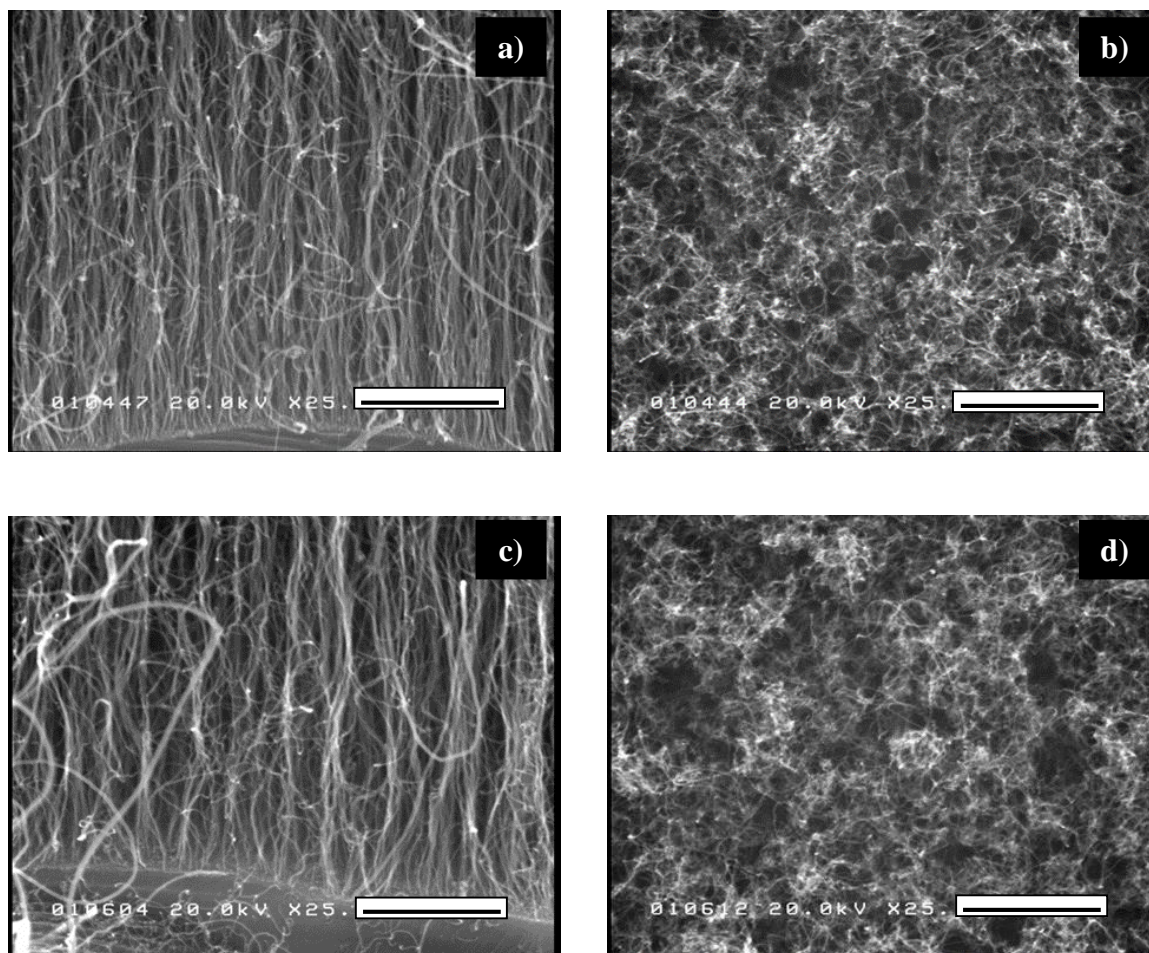


FIG. A.1. SEM images of samples of similar height of 25 microns, but different ferrocene concentration, a) Al/Si 127 base/side view, b) top view visibly more dense than c) Al/Si 132 base/side view, and d) top view. Scale bar 1.2 μm .

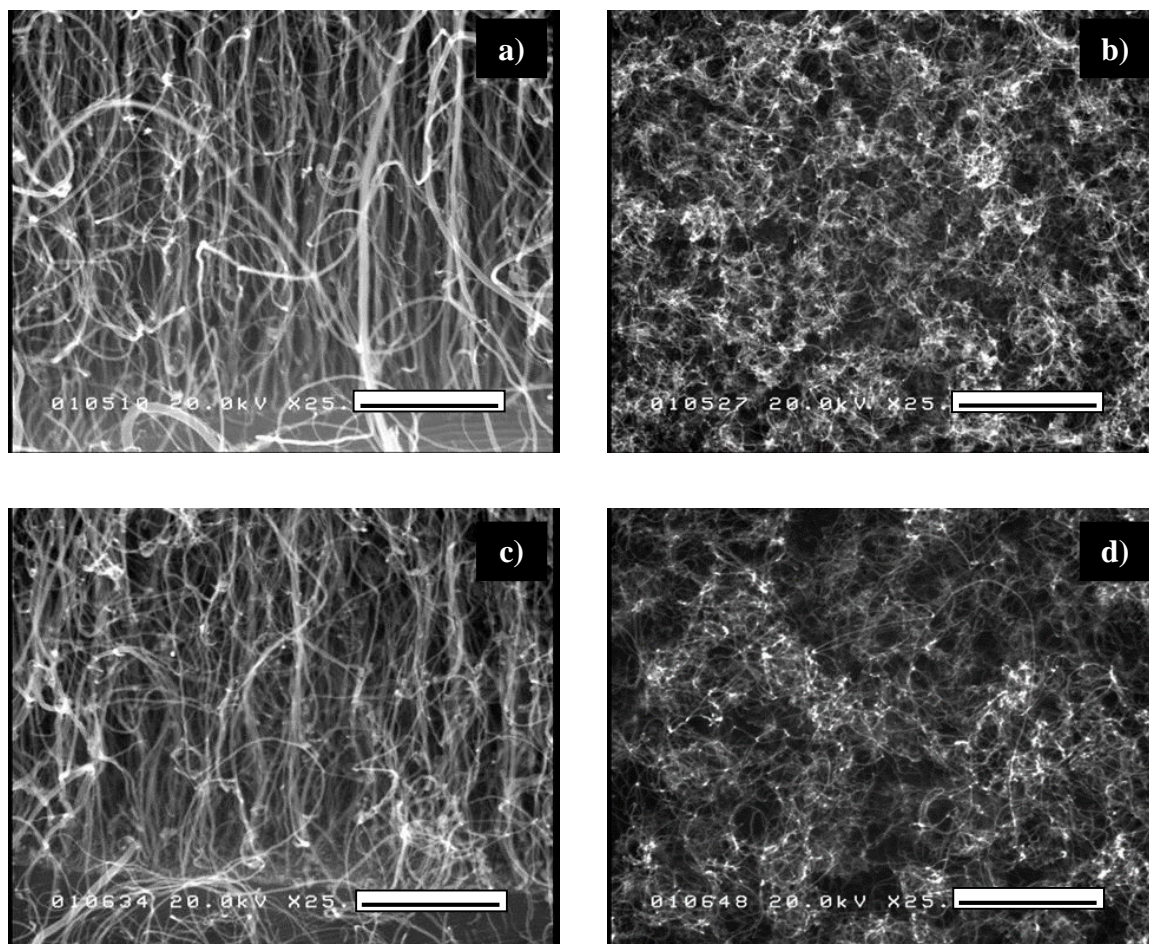


FIG. A.2. SEM images of samples with similar height around 45 microns, but different ferrocene concentrations. Al/Si 129 a) base/side view, and b) top view visibly denser than c) Al/Si 133 base/side view, and d) top view. Scale bar 1.2 μm .

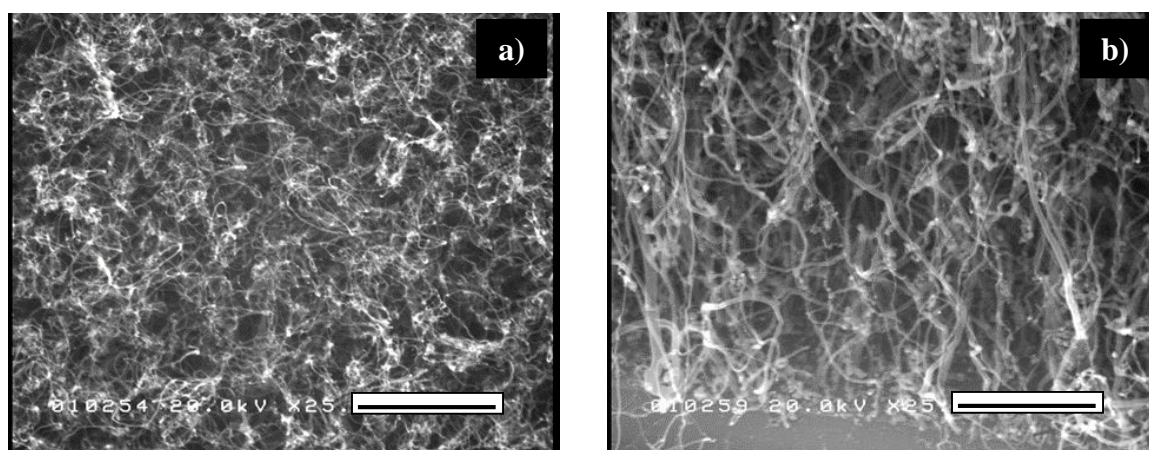


FIG A.3. Highly dense sample Al/Si 124 a) base/side view showing catalyst particle defects, and b) top view showing entanglement. Scale bar 1.2 μm .

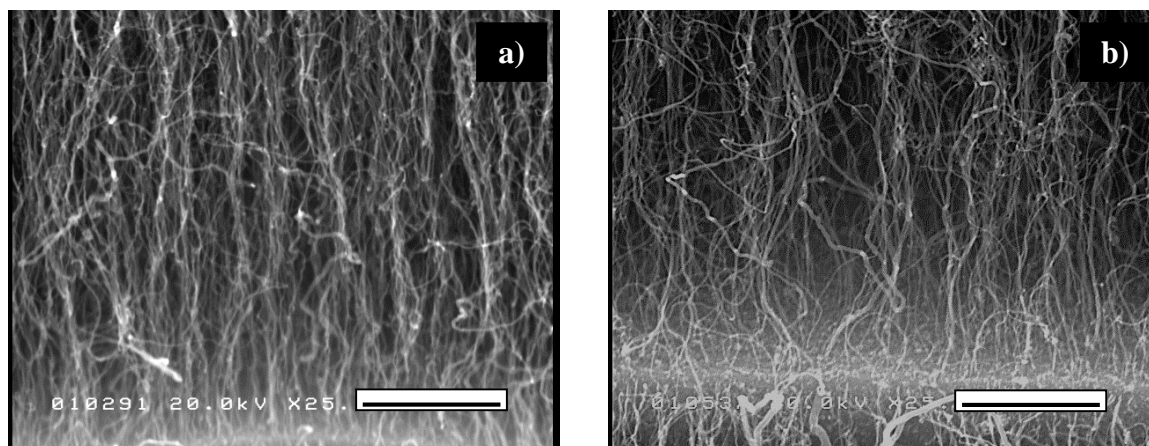


FIG A.4. Base, side views comparing the denser a) Q 125 with b) Q 130. Scale bar 1.2 μm .

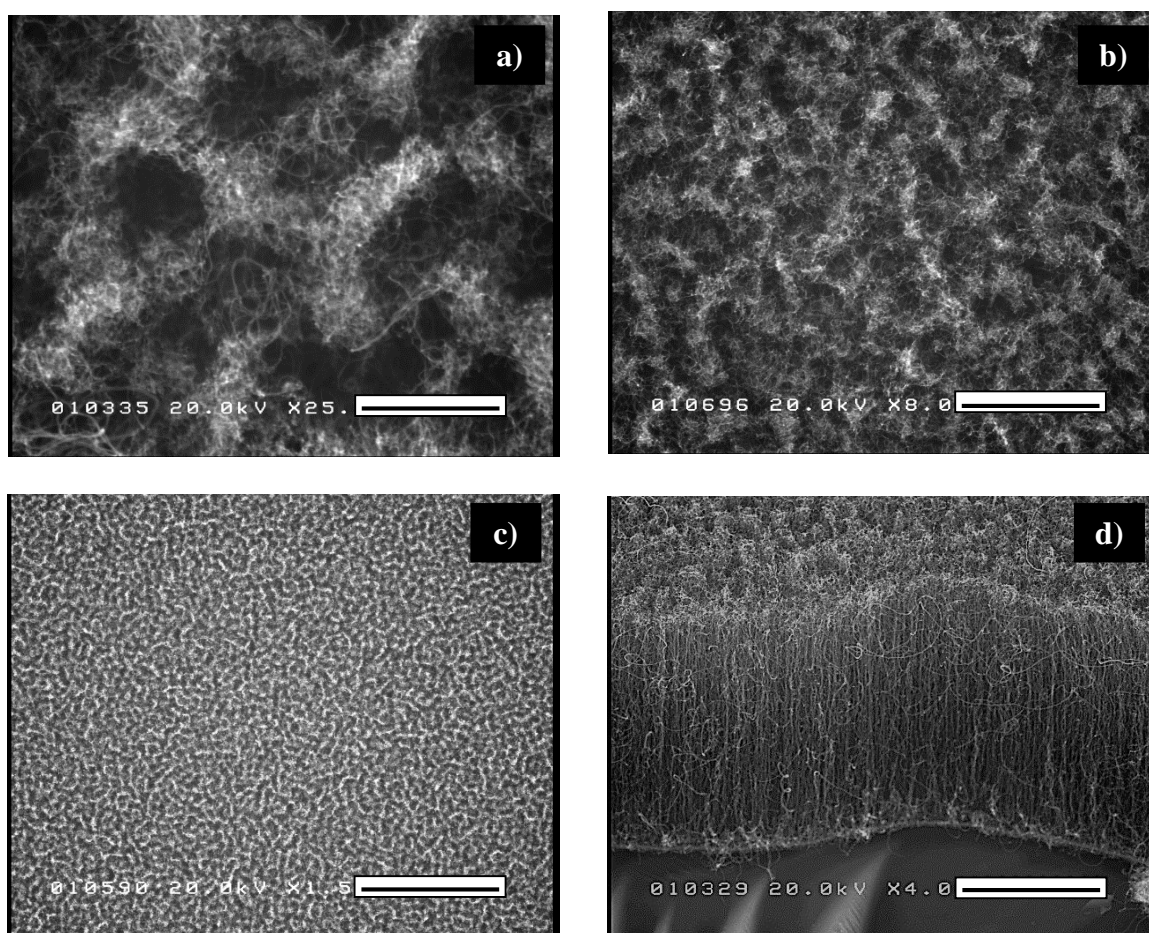


FIG A.5. Displaying top surface corrugation on successively different scales of a) Al/Nb 126, scale bar 1.2 μm , b) Al/Nb 135, scale bar 3.75 μm , c) Al/Nb 131, scale bar 20 μm , and a side view of d) Al/Nb 126, scale bar 7.5 μm .